MAX-PLANCK-INSTITUT
FÜR PHYSIK

Technische Universität München

Thesis submitted for the academic degree Bachelor of Science

Characterization of a prototype silicon drift detector for the IAXO experiment

Charakterisierung eines Prototyp Siliziumdriftdetektors für das IAXO Experiment.

Juan Pablo Ulloa Beteta

03712792

July 18, 2022

Primary reviewer: Prof. Dr. Susanne Mertens

Secondary reviewer: ....

Supervisor: Dr. Frank Edzards

Contents

1 Introduction

Since the dawn of civilization, humanity has been refining its understanding of the fundamental principles of reality. Hundreds of years of research have culminated in the Standard Model of Particle Physics, humanity's most successful theory for describing the building blocks of our Universe. It depicts the Universe as a collection of twelve different matter particles interacting with three different forces. However, the Standard Model is not a complete as it cannot explain the origin of Dark Matter and Dark Energy, nor does it incorporate gravity. In fact, Dark Matter and Dark Energy are thought to constitute 95% of our Universe. This means that only 5% of our Universe is conventional matter [1].

Another shortcoming of the Standard Model is the strong CP problem. In contradiction to the predictions of the Standard Model, experiments have never observed a violation of the Charge-Parity-symmetry by the strong interaction. Roberto Peccei and Helen Quinn proposed a solution in 1977. It constitutes a extension to the Standard Model that leads to the generation of a particle called the axion. Since then, various modifications to the original Peccei and Quinn solution have resulted in a vast range of axion-like particles of varying masses and properties. In general, axions are low-mass and very weakly interacting particles that could convert into photons in the presence of strong magnetic fields. Their existence would not only solve the strong CP-problem, but would also provide a candidate for cold dark matter.
Based on its properties, the axion would be produced in large quantities in the hot dense core of stars. This makes our sun the biggest source of axions from our perspective. Experiments such as the proposed International Axion Observatory (IAXO) attempt to detect solar axions by directing a powerful magnet towards the sun. Inside the magnetic field, axions convert into X-ray photons. The photons are then focused onto a low-background detector by an X-ray telescope. The detector system is required to have excellent energy resolution in the keV range, high X-ray detection efficiency and most important, an ultra-low background. The Silicon Drift Detectors (SDDs) from the TRISTAN project are detectors that have the potential to meet all of these requirements [2].

In the scope of this thesis, a background demonstrator for the TRISTAN SDD was developed with the goal of approaching the background requirements of IAXO. Initially, two detector boards were designed and subsequently tested extensively. Particular consideration was given to how a longer distance between the SDD and the readout electronics affects its performance. The insights gained from this analysis were then used to design a final detector board with dedicated shielding, which will be used in an upcoming background measurement. The detector boards were analyzed using photons from a ^{55}Fe calibration source to characterize the SDD. The data was analyzed using a classical pulse shape analysis approach that involves the processing of the individual signal events. The noise characteristics of each board were analyzed using the baseline root mean square as well as the resolution for various shaping parameters. For the final design, a resolution of $269 \pm 9\,\mathrm{eV}$ was achieved, which is sufficient for the background demonstration. A strong correlation between the signal rise time of a detector board and its distance between SDD and the readout electronics is found, which is not critical for the intended low-rate application.

2 Axion theory

Axion-like particles are a broad class of hypothetical generic pseudo scalar particles that satisfy the definition of weakly interacting slim particles (WISPs), they rarely interact with conventional particles and thus compete as candidates for cold dark matter [3].

2.1 Peccei-Quinn-Weinberg-Wilczek axion

One well motivated example is the PQWW (Peccei-Quinn-Weinberg-Wilczek) axion. It is a consequence of the PQ-Mechanism introduced by Roberto Peccei and Helen Quinn in 1977 in order to solve the strong CP-Problem.

2.1.1 Strong CP-Problem

The CPT theorem states that all physical phenomena must conserve the combined CPT symmetry [4]. Charge conjugation C, parity transformation P and time reversal T are discrete symmetry operations that change the initial state of a system, depending on its invariance properties. The effect of C is to replace a particle with its antiparticle $C : q \to \bar{q}$, P represents a spatial inversion through the origin $P : \vec{x} \to -\vec{x}$ and T is a reversal of the time coordinate $T : t \to -t$.

In theoretical physics, quantum chromodynamics (QCD) is the theory of the strong interaction between quarks and gluons that make up hadrons such as the neutron or proton. According to the mathematical formulation of QCD, its vacuum structure generates a CP violating term in the QCD lagrangian. More specifically, the QCD lagrangian has a term (Eq. 1), the Chern-Simons term, which is controlled by a phase parameter θ_{QCD} which violates parity and time reversal invariance, but conserves charge conjugation invariance, thus CP is violated.

$$\mathcal{L}_{\theta\mathrm{QCD}} = \frac{\theta_{\mathrm{QCD}}}{32\pi^2}\mathrm{Tr}(G_{\mu\nu}\tilde{G}^{\mu\nu}) \tag{1}$$

Here, G denotes the gluon field strength tensor and $\tilde{G}^{\mu\nu} = \epsilon^{\alpha\beta\mu\nu}G_{\alpha\beta}$ its dual tensor with ϵ_{ijk} being the Levi-Civita symbol [5].

The parameter θ_{QCD} defines the choice of vacuum. One also can think of θ_{QCD} as an amount of CP violation. Non-zero values for θ_{QCD} imply CP-violating observables, since in quantum field theory (QFT) operators give rise to all terms with the same symmetry. One well examined observable is the neutron's electric dipole moment (EDM), d_n, it is computed to be: $d_n \approx 3.6 \cdot 10^{-16}\theta_{\mathrm{QCD}} e\,\mathrm{cm}$ [6].

In our Universe the strong force seems to conserve CP symmetry, which in fact is exactly the problem. As a reminder, the neutron should have a magnetic dipole moment, but to our surprise the experimental evidence for such a dipole moment is missing, excluding its existence with an experimental limit ten orders of magnitude below the expected value [7]. As a consequence: $\theta_{\mathrm{QCD}} \leq 10^{-10}$. Beyond that, no experiment has ever observed CP violation in QCD [8]. To agree with the measurements of the non-observed CP violation, we would need to set θ_{QCD} to zero in Eq. 1.

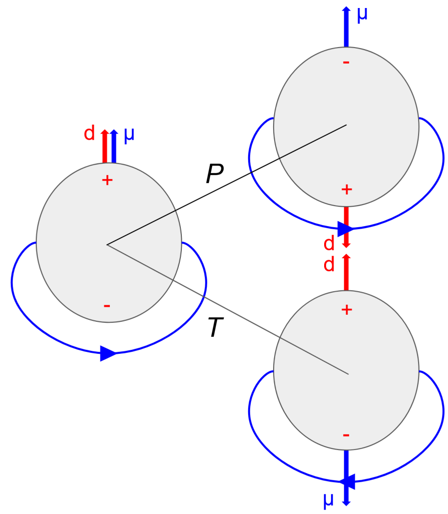

Figure 1: The electric dipole moment of the neutron d_n violates P and T invariance. Partiy transformation flips the electric dipole d. Time reversal flips the the magnetic moment μ. Consequently, a combined PT transformation does not restore the initial sate, resulting in a PT symmetry violation. Since the CPT theorem states the conservation of CPT, CP must be violated.

If we consider that θ_{QCD} consists of two separate parts of the Standard Model:

$$\theta_{\mathrm{QCD}} = \tilde{\theta}_{\mathrm{QCD}} + \arg(M_u M_d), \tag{2}$$

then the smallness of θ_{QCD} seems puzzling and results unnatural. $\tilde{\theta}_{\mathrm{QCD}}$ is a "bare" QCD contribution, while $M_u M_d$, the quark mass matrices, originate from the electroweak sector [5] and account for the quark mass spectra, flavor mixing angles and are known to violate CP [9].

For θ_{QCD} to be zero, both dimensionless terms which emerge from different physics, have to cancel out exactly. This seems highly improbable. We arrive at something that is known as a fine tuning problem, in this case the strong CP- problem [10]. The smallness of CP-violation gives us a hint for a dynamical mechanism that suppresses the effects of θ_{QCD} in the equation.

2.1.2 The Peccei Quinn Mechanism

The Peccei and Quinn mechanism is a proposed solution to the strong CP-problem [11]. Rather than assuming θ_{QCD} to be constant at zero, it is explained via a dynamical CP-conserving field, i.e. making θ_{QCD} a dynamical variable, which itself gives rise to the existence of the axion.
The theory introduces a complex scalar field φ and a global chiral anomalous $U(1)_{\mathrm{PQ}}$ symmetry which is broken at the energy scale f_a by φ. With this approach the vacuum angle θ_{QCD} will depend on the vacuum state and dynamically relax to the value that minimizes the vacuum, resulting in $\theta_{\mathrm{QCD}} = 0$ [4].

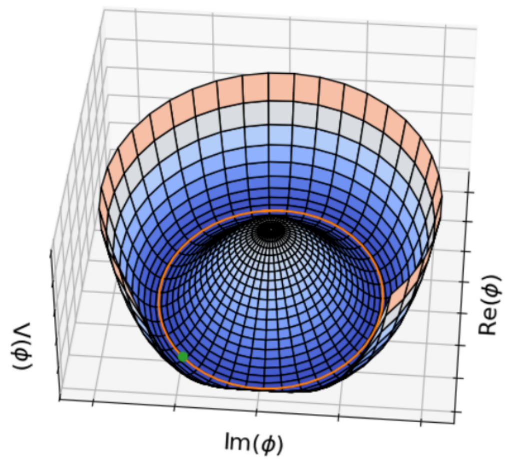

Figure 2: Schematic representation of the spontaneous symmetry breaking potential $V(\varphi)$. The axion (green dot) takes a random value between $[-\pi, \pi)$ and remains massless, it becomes a Nambu-Goldstone boson that oscillates inside the potentials brim. The $U(1)_{\mathrm{PQ}}$ symmetry is depicted as rotational symmetry in the complex plane. Adapted from [12].

The complex scalar field φ has the symmetry breaking potential:

$$V(\varphi) = \lambda \left(|\varphi|^2 - \frac{f_a^2}{2} \right)^2 \tag{3}$$

where f_a, the axion decay constant, is set to the electroweak scale to guarantee a behavior comparable with the Higgs field. The electroweak scale ν_F depends on the vacuum expectation value of the Higgs field which itself depends on the Fermi coupling constant G_F, resulting in $f_a \approx 246\,\mathrm{GeV}$. Temperatures below this scale invoke a non-zero vacuum expectation value of $\langle\varphi\rangle = f_a/\sqrt{2}$, provided by the spontaneous symmetry breaking potential $V(\varphi)$ [5]. Here, spontaneously broken means that all states of the theory share the symmetry except for the ground state. This results in $V(\varphi)$ adopting the characteristic shape of "Mexican hat", visible in Fig. 2

The required spontaneous symmetry breaking of the $U(1)_{\mathrm{PQ}}$ symmetry below the electroweak scale is associated with the appearance of Nambu-Goldstone (NG) boson ϕ, the axion [10]. This was postulated by Weinberg and Wilczek independently. It is an angular degree of freedom at the bottom of the potential with a shift symmetry, which allows us to shift the axion field φ by an arbitrary constant. Therefore, the value of θ_{QCD} can be absorbed by ϕ into a redefinition of the axion field, effectively θ_{QCD} gets rotated away.

As soon as temperatures reach a critical point, $T_c = 170 - 200\,\mathrm{MeV}$ [13], QCD effects come into play, giving the axion a mass [12]. The axion becomes a pseudo-Nambu-Goldstone boson. Consequently, the potential is slightly tilted, causing θ_{QCD} to minimize along the preferred axis and move to the fixed value of zero by symmetry, depicted in Fig. 3.

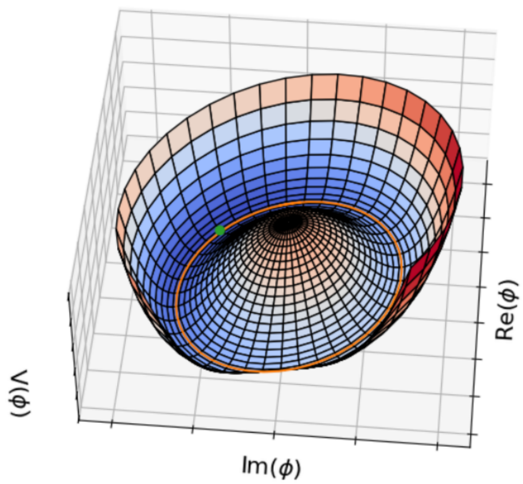

Figure 3: For temperatures $T \ll T_c$, QCD tilts the potential $V(\varphi)$. In the tilted "Mexican hat" potential, the axion field adapts a preferred CP conserving value (green dot). Angular oscillations around $\theta_{\text{QCD}} = 0$ represent a massive axion particle, whereas radial oscillations represent a very heavy particle at the scale of f_a. Adapted from [12].

In other words, θ_{QCD} must be minimized since any other value of θ_{QCD} would require energy. The minimized θ_{min} eliminates the neutron's electric dipole moment and thus solves the strong CP-problem.

2.2 Axions properties

As previously described, the axions originates from the PQ mechanism, which is a solution to the strong CP problem. Furthermore, the PQ mechanism establishes some of the axion's properties, which are therefore independent of the particular axion model [12]. This includes the axion mass m_a and its coupling constant to other particles, g_{ai} [8]:

$$m_a \propto \frac{1}{f_a}, \;\; g_{ai} \propto \frac{1}{f_a}. \tag{4}$$

The axion mass m_a and coupling constant g_{ai} depend on the $U(1)_{PQ}$ symmetry breaking scale f_a, hence different values produce axions with distinct mass and coupling strength. Small values of f_a produce axions with observable mass, which are referred to as visible axions. Axions with large f_a values are almost non-observable, so they are referred to as invisible Axions [8]. Axion couplings to gluons and photons occur in all theoretical models, unlike couplings to fermions and quarks, which vary depending on the model.

2.2.1 Axions models

Visible axions

For the original PQWW axion the symmetry breaking was set to the electroweak scale, as a matter of fact, it is not necessary since f_a can have an arbitrary value [10]. Therefore, $f_a = \nu_F \approx 246\,\mathrm{GeV}$, corresponding to a visible axion a with a mass of $m_a \approx 100\,\mathrm{keV}$ [8]. The mass is generated automatically by QCD and thus only depends on f_a [12].

However, the idea of such an axion has been rejected as there has been no experimental support of such a mass. Furthermore, as a result of the following flavor violating rare decay mode of stopped kaons, this should have resulted in a detection at accelerators:

$$K^+ \to \pi^+ a. \tag{5}$$

In spite of that, such a decay has never been observed [14].

Invisible axions

In agreement with current experimental constraints, it is necessary to build models, in which $f_a \gg \nu_F$. This would yield very light, almost non-interacting, and very long-lived axions. Therefore, this group is named invisible axions [10].

The family of invisible axions can be divided into two models: the Kim-Shifman-Vainshtein-Zakharov (KSVZ) Model and the Dine-Fischler-Srednicki-Zhitnisky (DFSZ) Model. The axion resulting from the KSVZ model is hardronic, whereas the DFSZ models is non-hadronic.

The KSVZ Model suggests a different realization than the PQ-mechanism, the biggest difference being the introduction of a $U(1)_A$ symmetry, additional scalars and a very massive quark ψ with $m_\psi \sim f_a$ [15], all of which are neutral with respect to electroweak interactions. The resulting KSVZ axion is nearly sterile, meaning that it does not couple to ordinary quarks and fermions at the tree level, only to photons. Couplings to ordinary quarks are only possible through the introduced heavy quark ψ when the $U(1)_A$ symmetry is broken [16], therefore allowing the coupling to hadrons. Kim estimated the axions mass to be $2.7\,\mathrm{eV}$ [16].

On the other hand, the DFSZ model is almost identical to that of Peccei and Quinn, the only modification being the addition of a complex scalar field ϕ, accompanied by two scalar doublets ϕ_u and ϕ_d. The former is required to only couple to u-type quarks, while the latter only couples to d-type quarks and leptons [17]. Effectively, the Higgs field gets substituted by two new ones [8], giving mass to the W and Z bosons, quarks and leptons. Furthermore, SM fermions will carry PQ charges, which induces axion-electron coupling at the three level, i.e $g_{ae} \neq 0$. The mass of such an axion is computed to be $m_a \simeq 74\,\mathrm{keV}(250\,\mathrm{GeV}/f_a)$ [17].

2.2.2 Axion couplings

As previously stated in Eq. 4, all axion couplings are inversely proportional to the symmetry breaking scale f_a. This relation originates from the axion Lagrangian:

$$\mathcal{L}_a = \xi \frac{g^2}{32\pi^2} G^a_{\mu\nu} \tilde{G}^{\mu\nu}_a \frac{a}{f_a} - \frac{1}{2} \partial_\mu a \, \partial^\mu a + \mathcal{L}(\partial_\mu a, \psi). \tag{6}$$

The first term describes the axion potential energy where ξ denotes a model-specific constant and a the axion field. The second term defines the kinetic energy of the axion field, while the third term describes the interactions between the axion field and fermions [8]. As can be seen from Eq. 6, axions can couple to the gluon field independent of the model and mix with neutral mesons. Furthermore, the coupling to photons is possible through the mixing process itself [12].

Axion-gluon coupling

The most generic property of the axion is the axion-gluon coupling. It is implied by the axion Lagrangian, see Eq. 6, in which the axion field couples to the gluon field. The coupling strength is inversely proportional to the symmetry breaking scale f_a. Due to the axion-gluon interaction, the mixing with pions which have the same quantum numbers as axions, is enabled [8], as in Eq. 5.

Axion-photons coupling

Of particular interest from the experimental point of view is the coupling of axions to photons. It is an essential consequence of the PQ mechanism and thus model-independent.
The effective axion-photon Lagrangian is given by

$$\mathcal{L}_{a\gamma\gamma} = \frac{1}{4} g_{a\gamma\gamma} a \, F_{\mu\nu} \tilde{F}^{\mu\nu}, \tag{7}$$

where $g_{a\gamma\gamma}$ denotes the coupling constant, $F_{\mu\nu}$ the electromagnetic field tensor and $\tilde{F}^{\mu\nu}$ its dual. The coupling constant $g_{a\gamma\gamma}$ is strongly influenced by the axion model, specifically the assignment of PQ charge. It is possible to build models that result in both suppressed and enhanced photon-axion couplings [18].

For a real photon and a static magnetic field, one finds

$$\mathcal{L}_{a\gamma\gamma} = g_{a\gamma\gamma} a \, \vec{E} \cdot \vec{B}_{\text{ext}} \tag{8}$$

where $\vec{E}$ and $\vec{B}_{\text{ext}}$ are the electric and magnetic field, respectively. As indicated by Eq. 8, the axion exclusively interacts with the photon wave component parallel to the external magnetic field [18]. Photons will be able to oscillate in strong electric or magnetic fields into axions or vice versa, this process is known as Primakoff effect, shown in the Feynman diagram in Fig. 4.

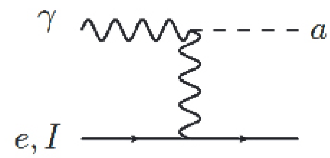

Figure 4: The coupling of axions to a virtual and a real photon is known as the Primakoff effect. It occurs when an axion is in the presence of an strong electric or magnetic field, which can be seen as the virtual photon. Adapted from [19]

This process proves to be extremely useful for experimental approaches, allowing to convert axions into detectable photons. The coupling results as [20]:

$$g_{a\gamma\gamma} \sim 10^{-3} \frac{\mathrm{GeV}^2}{f_a}. \tag{9}$$

Axion-nucleon coupling

The mixing of the axion with mesons yields a model-independent coupling to nucleons. On the other hand, depending on the model, axions can feature an axion-quark coupling. For the KSVZ model this is possible. The general coupling can be expressed as:

$$g_{af} = C_{af} \frac{m_f}{f_a}, \tag{10}$$

where C_{af} corresponds to the dimensionless axion-fermion coupling. It depends on the particular fermion and has both model dependent and independent contributions. As will be discussed below, nucleon couplings play an important role in some astrophysical scenarios and are thus relevant when constraining axion models [12].

Axion-electron coupling

The axion-electron coupling is only important for the DFSZ model since there fermions carry PQ charge, allowing for tree-level couplings, described by:

$$g_{ae}^{\mathrm{tree}} = C_e \frac{m_e}{f_a}, \tag{11}$$

where C_e stands for the electron's effective PQ charge and is therefore a model-dependent coefficient. Relevant processes include [19]:

- Electron-ion bremsstrahlung (ff)

$$e + I \to e + I + a$$

- Electron-electron bremsstrahlung (ee)

$$e + e \to e + e + a$$

- Compton scattering (photo-production) (C)

$$e + \gamma \rightarrow e + a$$

- atomic axio-recombination (bf)

$$e + I \rightarrow I^- + a$$

These processes are severely restricted by astrophysics, as will be discussed in the next section.

2.2.3 Axions constraints and parameter space

The axion search is discussed in a two-dimensional parameter space, with the axion mass m_a and the coupling to the photon $g_{a\gamma\gamma}$ as axes. Both $g_{a\gamma\gamma}$ and m_a are related by f_a, see Eq. 4, therefore constraints on either affect both. Figure 5 depicts a representation of this parameter space with all relevant constraints.

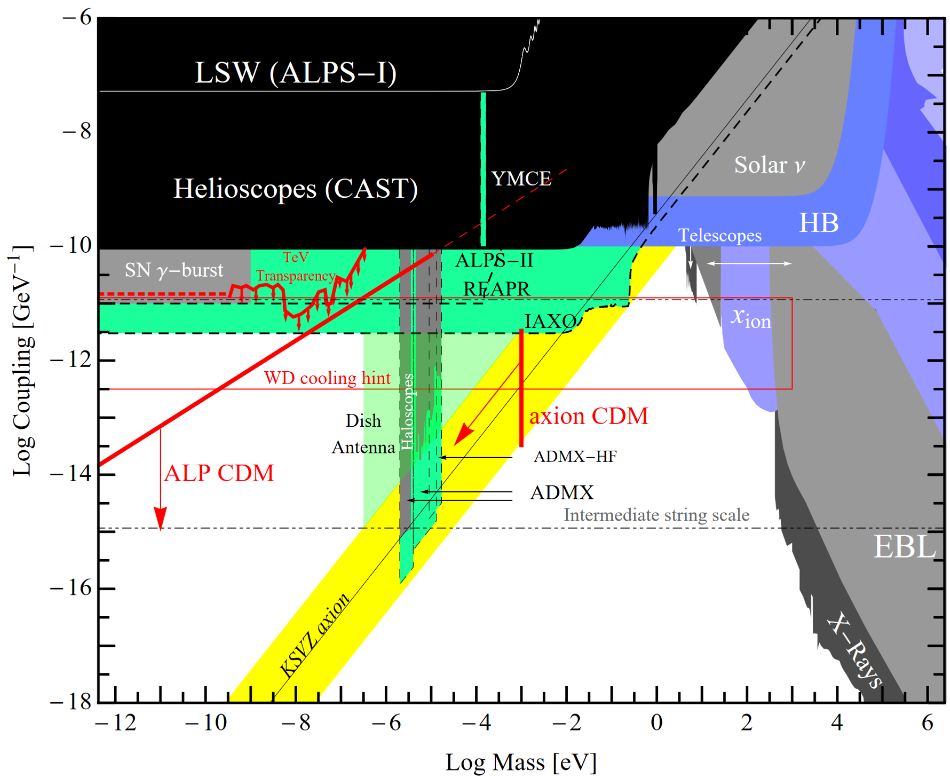

Figure 5: Parameter space for axion-like particles ALPs: coupling to photons vs their mass. The QCD-motivated axion models lie within the yellow band and the KSVZ line respectively. (black): experimentally excluded regions, (gray): constraints from astronomical observations, (blue): constraints from astrophysical or cosmological arguments, (red): hints for axions and ALPs from astrophysics, (light green): sensitivity of planned experiments. Adapted from [21].

In theoretical models, the value for the symmetry breaking scale f_a, and thus for m_a and g_{ai}, is rather arbitrary. The couplings mentioned above would result in the production of axions, primarily via the Primakoff effect, in hot and dense environments, such as stars, globular clusters and white dwarfs [8]. Astronomical observations of the standard stellar-cooling mechanism impose strict limits on axion couplings to photons, electrons, and nucleons. In particular, stars would lose energy due to axion emission, resulting in a vast increase in the stellar cooling speed [19] and observable modifications in the properties of individual stars or entire stellar populations [22].

Furthermore, the Sun would become a powerful axion source which helioscopes, such as the CAST experiment, can take advantage of. Most values of $f_a \lesssim 10^9\,\mathrm{GeV}$ are ruled out by a direct search for such particles or calculations of their effect on star cooling [20].

Beyond that, the introduction of non-hadronic axions that couple to electrons could explain the delayed helium ignition of red giants of the globular cluster Messier 5, since the emission of low-mass particles would provide additional cooling of the helium core and thus increase the necessary core mass before the helium ignites. Observations of Messier 5 set an upper limit for the electron coupling of $g_{ae} < 4.3 \cdot 10^{-13}$ [22].

Other astrophysical puzzles, such as the non-standard cooling rate of white dwarf stars such as the ZZ Ceti star G117-B15A and the anomalous transparency of the universe for TeV gamma rays, may be solved by the existence of axions [20], constraining the axion's parameter space further. The latter could be explained by photon-axion oscillation, in which gamma photons convert into axions and travel unimpeded for large cosmological distances before reappearing near us via re-conversion in large-scale astrophysical magnetic fields.

Finally, cosmology establishes a lower bound on axion mass and an upper bound on f_a. This results for the WMAP data [23] in: $f_a < 3 \cdot 10^{11}\,\mathrm{GeV}$ and $m_a > 2.1 \cdot 10^{-5}\,\mathrm{eV}$ [10]. Taking all relevant constraints into account, the parameter space shown in Fig. 5 is obtained.

2.3 Axion-like particles

A whole class of particles known as Axion-Like Particles (ALPs) is motivated by various extensions of the SM, they satisfy the criterion of Weakly Interacting Slim Particles (WISPs). As pseudo Nambu-Goldstone bosons of a broken symmetry at high energy scales, ALPs and axions result as light pseudo-scalar particles that couple to two photons. Certain string theory-based extensions of the SM predict a wide range of ALPs [24]. Since ALPs are not motivated by QCD, they will not necessarily couple to gluons. In addition, their mass and coupling constant will be independent parameters, giving them access to the whole parameter space [8] illustrated in Fig. 5.

2.4 Dark Matter

Cosmological observations revealed that the Universe is dominated by "dark" components, the presence of which can only be witnessed through their gravitational effect. In particular, cosmological models demand the addition of two new substances, Dark Energy and Dark Matter (DM). The Standard Model does not account for either. DM is thought to account for 27% of the known universe, while conventional matter accounts for only 5% [1]. The first experimental evidence for dark matter was discovered as early as 1933 by F. Zwicky [25]. This investigation indicated discrepancies between expected and observed orbital velocities of galaxies near the edges of galaxy clusters. In essence, the gravitational effects of the visible galaxies were too small to account for the fast orbits of the galaxies near the edge. DM could represent the mass associated with the gravitational attraction required to hold the cluster together. Further evidence comes from the cosmic microwave background radiation temperature anisotropies [26] and observations of the gravitational lensing around galaxy cluster cores [27].

Popular particles that could constitute DM are "Weakly Interacting Slim Particles" (WISPs), of which the axion and ALPs are well motivated [21]. To constitute cold DM, axions need to be produced non-thermally in the early universe. This could have been realized through the vacuum-realignment mechanism, which is closely connected to the PQ mechanism [12]. It is based on the fact that the initial θ_{QCD} and θ_{min} generally differ, resulting in a misalignment between the two. As soon as the QCD effects engage, the axion falls to its minimized position, beginning a dampened oscillation around it. The oscillations coincide with a coherent state of non-relativistic axions that could constitute cold DM, filling the space with a cold axion population. The small mass of the axion would result in a huge phase-space density, allowing the formation of a Bose-Einstein condensate and, eventually, massive structures in the galactic halo [21].

3 Experimental searches for axions and ALPs

The experimental search for axions or ALPs proves to be challenging due to the properties of these particles. In particular, the feeble interaction with matter requires a different approach than collider experiments. For the direct detection of axions, there are three main approaches: haloscopes look for DM axions from the galactic halo; Light-Shining-Through-Wall (LSW) experiments look for axions produced in the laboratory; and lastly, helioscopes look for solar axions. All of these methods rely on the Primakoff effect to convert photons to axions in strong magnetic fields, which is explained in Ch. 2.2.2.

3.1 Haloscope experiments

The haloscope method was first proposed in 1983 by P. Sikivie [28] and aims to detect cold DM axions potentially originating from the galactic halo. These axions are produced in the early Universe by the vacuum realignment mechanism (Ch. 2.4) and are theorized to have masses of $10 - 200\,\mu$eV. A haloscope is a cryogenic cavity detector comprised of a tuneable resonant cavity that is immersed in the strong magnetic field of a superconducting solenoid and a receiver with an ultra-low noise pre-amplifier [29]. A representation of the ADMX haloscope is depicted in Fig. 6.

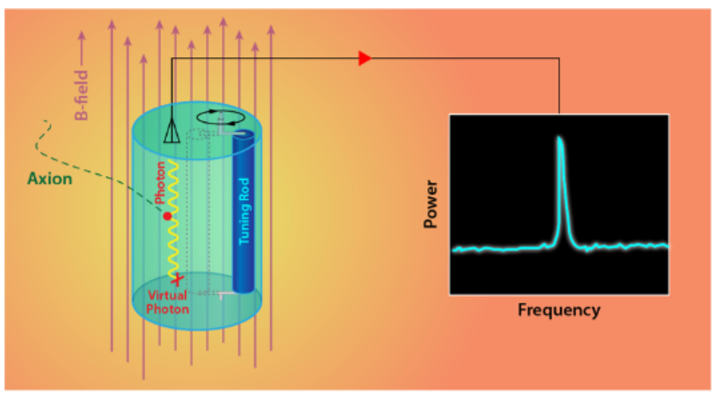

Figure 6: Conceptual design of the ADMX haloscope. A superconducting solenoid's strong magnetic field surrounds the resonant cavity. The resonant frequency can be adjusted by the moving the tuning rods inside the cavity. If the resonant frequency matches the mass of the axion, the conversion rate of axions to photons is significantly enhanced, depositing excess energy. Adapted from [8].

Unlike photons from solar axions, photons from DM axions can be considered monochromatic in energy, since the energy of DM axions only corresponds to their mass. As a result, the conversion into photons can be optimized by employing a resonator with a frequency peak that corresponds to the energy of the produced photons which is equal to the mass of the incoming axion [21].
When a DM axion enters the static magnetic field, it couples to it and converts into a microwave photon, depositing excess power [30]. This happens only if the resonant frequency is close to the mass of the axion. The frequency can be adjusted by moving a pair of axial tuning rods from the

center of the cavity to its wall [31]. By tuning for different resonant frequencies it is possible to probe different axion masses. The state of the art haloscope is the Axion Dark Matter eXperiment (ADMX). The collaboration used a 100 cm-long resonant frequency cavity with a diameter of 50 cm immersed in a 7.9 T field, to exclude KSVZ halo axion of mass $1.9-3.3\,\mu$eV [31]. These limits were supplemented by the incorporation of a Superconducting QUantum Interference Device (SQUID) amplifier, excluding KSVZ DM axions with masses ranging from $3.3-3.53\,\mu$eV [32].

3.2 LSW experiments

Light-Shining-through-a-Wall (LSW) experiments rely on axions produced in the laboratory. The basic components of such an experiment are a powerful laser in front of a light-blocking barrier and a detector behind that barrier. The space between the laser and the barrier, as well as the space between the barrier and the detector, is surrounded by a strong magnetic field. The laser photons are converted inside the magnetic field via the Primakoff effect into axions and can thus pass through the barrier unimpeded. The laser beam provides the real photon, while the magnetic field provides the virtual photon. Behind the barrier, the axions get reconverted analogously into photons, which can then be measured by the detector, effectively shinning light through a wall [33]. A representation of the ALPS-I LSW experiment is depicted in Fig. 7.

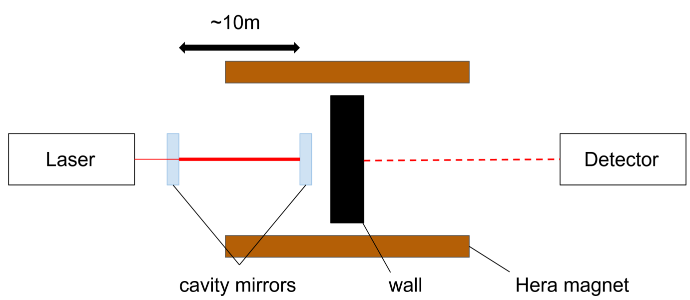

Figure 7: Conceptual design of ALPS-I at DESY. ALPS-I has a 10 m long production cavity that is surrounded by a HERA superconducting dipole magnet and has cavity mirrors on both sides to effectively increase the production area. Inside the magnetic field, laser photons are converted into axions which pass through the barrier. The axions are converted back into photons behind the barrier, which can then be measured by the detector.

For the ALPS-I experiment it was possible to establish a limit for the photon coupling of $g_{a\gamma\gamma} < 6.5 \cdot 10^{-8}\,\mathrm{GeV}^{-1}$ for axion masses $m_a < 1\,\mathrm{meV}$ [34]. The proposed ALPS-II experiment aims to exceed current helioscope limits by incorporating an optical resonator that amplifies the laser light power by storing the injected laser light. Furthermore, by arranging multiple dipole magnets together, the magnetic length will be increased [35]. Current LSW experiments are not as sensitive as helio- or haloscopes, but the advantage is the complete control over WISP production which eliminates the need for astrophysical or cosmological assumptions [21]. Furthermore, because the Primakoff conversion must occur twice, their sensitivity is reduced [8].

3.3 Helioscope experiments

As previously stated in Ch. 2.2.3, axions should be produced in large quantities in the interior of our sun through the Primakoff conversion of blackbody plasma photons in the fluctuating Coulomb fields of charged particles in the sun's plasma. This makes our sun the brightest source of solar axions from our perspective. P. Sikivie was the first to propose the heliscope method [28]. It searches for solar axions by directing a strong dipole magnet towards the sun, allowing the axions to be reconverted into detectable photons. The magnet provides for the virtual photons necessary for the Pimakoff effect. The converted photons have the same energy as the incoming axion. Because of this, incoming solar axions which have energies of order one keV [28], result in photons in the X-ray range. To reduce the signal-to-noise ratio, X-ray optics are used to focus the photons Onto a small spot. A low-background X-ray detector is located at the optics' focus point. As a result, when the helioscope is aligned with the sun, an excess of X-rays over the radioactive background measured at non-aligned periods is expected. In Fig. 8 the conceptual design of a helioscope is shown.

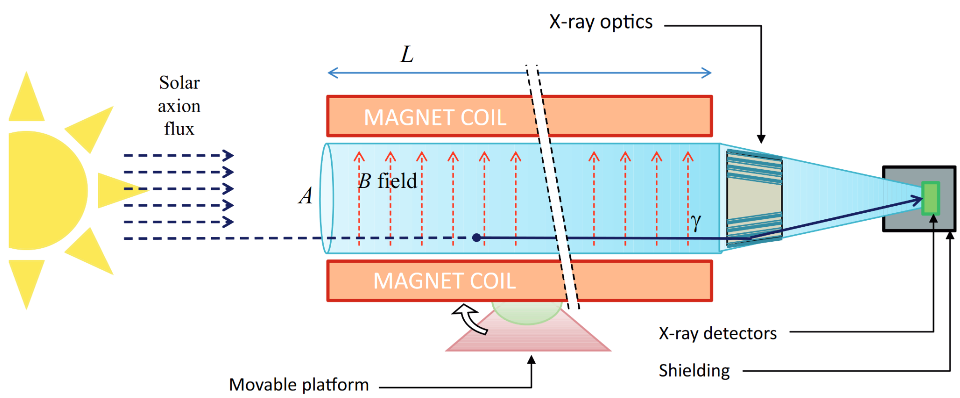

Figure 8: Conceptual design of a helioscope. A movable platform directs the heliscope towards the sun. Through the Primakoff effect, solar axions are converted into X-ray photons inside a strong magnetic field. The resulting photon beam is focused by X-ray optics into a small spot in a low-background detector. Adapted from [36].

In 1992, the concept of a helioscope was used for the first time by the Brookhaven National Laboratory. A 1.8 m long and 2.2 T strong magnet was used to to conclude an upper limit on the axion mass and photon coupling of $m_a < 0.03\,\mathrm{eV}$ and $g_{a\gamma\gamma} < 3.6 \cdot 10^{-9}\,\mathrm{GeV}^{-1}$ [37]. Helioscopes have matured to this day, allowing the CERN Axion Solar Telescope (CAST) to set new experimental limits, entering the QCD axion model band Fig. 5 and excluding KSVZ axions of specific mass values [36] for the first time. It uses a 9.3 m long, 9 T decommissioned LHC dipole magnet on a tracking mount and ultra-low background x-ray detectors. The proposed IAXO experiment [38] is the fourth generation of helioscope. By being 4–5 orders of magnitude more sensitive than CAST, it aims to improve the signal-to-background ratio.

Helioscopes have the advantage of being the most mature technology and covering axion masses in a wide range of parameter space, since the signal is independent of the axion mass, thus covering a broader class of models.

3.4 IAXO: International AXion Observatory

The International AXion Observatory, IAXO, is a proposed fourth-generation axion helioscope that will search for axions or ALPs originating in the Sun via the Primakoff conversion of solar plasma photons. As previously stated, the goal is to outperform CAST's sensitivity by four to five orders of magnitude. IAXO will be able to probe previously unexplored areas of the parameter space, reaching axion-photon couplings of a few $10^{-12}\,\mathrm{GeV}^{-1}$ for masses up to $0.25\,\mathrm{eV}$. Furthermore, for the first time, it is possible to be sensitive to solar axions produced by the axion-electron coupling g_{ae} for values previously not excluded by astrophysics [36]. IAXO is designed following the conceptual layout of an enhanced axion helioscope. It features a large superconducting magnet, X-ray optics and ultra-low background Micromegas X-ray detectors [8].

Furthermore, a prototype for IAXO is being developed, known as BabyIAXO. It is a scaled-down version of IAXO, with two 10 m-long magnet coils and X-ray optics and detectors similar to those expected in IAXO [39]. BabyIAXO is scheduled to begin operations in 2024. In the following sections, the individual components of IAXO will be discussed in detail. A schematic view of IAXO is depicted in Fig. 9.

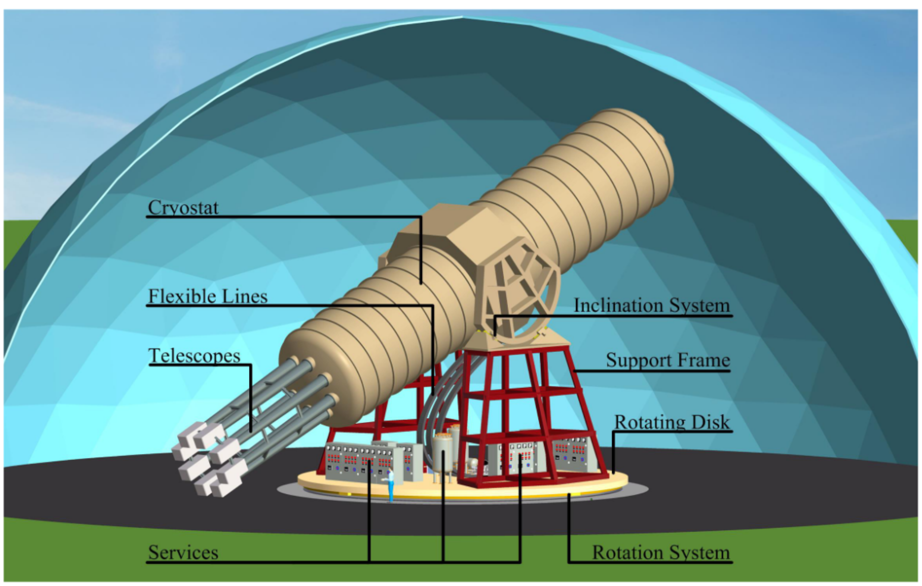

Figure 9: Schematic view of IAXO. Shown is the cryostat that houses the superconducting magnet and the eight X-ray optics with their corresponding low-background detectors. The telescope is mounted on an inclination/rotating system that allows it to track the sun. Adapted from [36].

3.4.1 Superconducting magnet

To achieve the stated experimental sensitivity, the IAXO experiment relies on the construction of a large superconducting magnet optimized for axion research. The current design foresees a 250 t heavy, 25 m long magnet with a diameter of 5.2 m. The magnet is composed of eight 21 m long and one meter wide racetrack coils in a torodial arrangement. Niobium–titanium is used as a superconducting material, allowing the magnet to reach a peak magnetic field of 5.4 T [38]. The magnetic field must be perpendicular to the longitudinal direction of incoming axions, since only the perpendicular components of B will contribute to the conversion probability, as discussed in Ch. 2.2.2. The decisive parameter that determines the performance of the magnet is the magnets figure of merit (MFOM), given by

$$f_M = L^2 B^2 A. \tag{12}$$

Here L denotes the length of the magnet, B the effective magnetic field and A the aperture covered by the X-ray optics. This value is optimized by positioning the X-ray optics as close to the toroid's inner radius as possible and aligning each optic between each pair of racetrack coils, known as "area dominated" alignment, see Fig. 10.

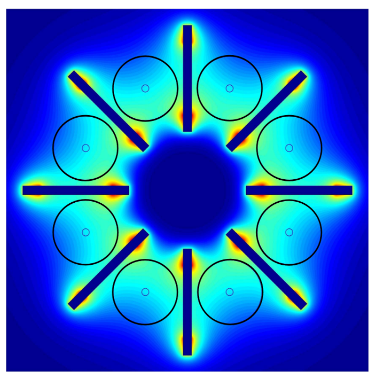

Figure 10: Illustration of the "area dominated" alignment, which takes advantage of each optic's entire aperture and thus optimizes the magnets figure of merit (MFOM). The rectangles represent the coils of the toroid, while the circles represent the telescope bores. Adapted from [36].

The cryogenic system that cools the magnet's coils employs sub-cooled liquid helium at a temperature of 4.5 K. This allows the maximum temperature rise in the coils to be limited to 0.1 K above the coolant temperature.

3.4.2 X-ray optics

The X-ray optics are intended to focus the generated X-ray signal to as small an area as possible. This reduces the detector's required size while increasing the signal-to-noise ratio. Each magnets features its own telescope. The X-rays produced by the Primakoff effect within the magnet are parallel to incoming axions. As a result, the telescope's field of view must be the size of the axions production region. This area corresponds to the sun's central core with 0.87 mrad. The telescope focuses the signal photons into a $\sim 0.2\,\mathrm{cm}^2$ spot. The optics have a focal length of 5 m and are based on grazing-incidence reflective optics. X-ray mirrors functioning at grazing incidence can focus X-rays over a wide energy range. Their reflectivity is limited by a critical angle beyond which the reflectivity significantly decreases [40]. For IAXO, this graze angle ranges from 2.63 mrad to 15.0 mrad. The telescope uses slumped glass as substrate that is coated with multiple layers of wolfram and boron carbide, which serve as reflective coatings. Furthermore, the telescope is segmented, meaning it consists of individual mirrors (2172 per telescope) [38]. A conceptual design of the optics can be seen in Fig. 11.

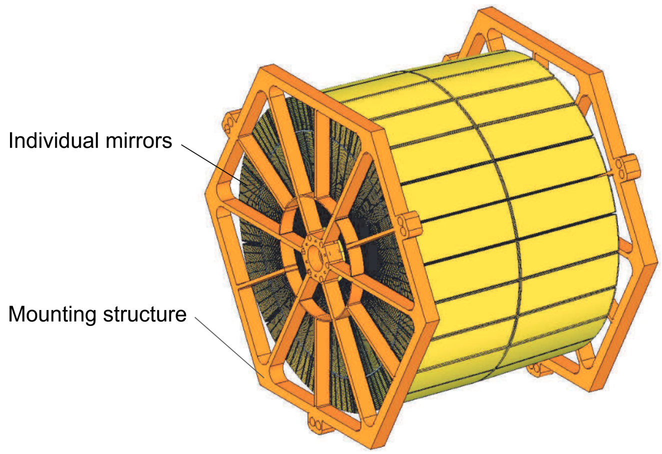

Figure 11: An isomorphic side-view of one X-ray telescope. IAXO adopted segmented, slumped glass optics, coated with reflective layers. Thousands of individual mirror segments can be seen. The hexagonal structure is responsible for mounting the optics to the magnet bores. Adapted from [36].

3.4.3 Micromegas X-ray detector

For IAXO the signal-to-background ratio in region of interest ($< 10\,\mathrm{keV}$) is critical to success. Micromegas detectors serve as the baseline for IAXO's low-background X-ray detectors. The Micromegas TPCs have reached a background level of $\sim 10^{-6}\,\mathrm{counts\,keV^{-1}\,cm^{-2}\,s^{-1}}$ in CAST and have the intent to reduce it to $\sim 10^{-7}\,\mathrm{counts\,keV^{-1}\,cm^{-2}\,s^{-1}}$ in IAXO [36]. They are Time Projection Chambers (TPCs), which are gaseous detectors filled with an Ar/isobutane mixture. The X-ray photons focused by the optics enter the detector through a thin window that further serves as cathode. Interactions in the gas produce primary electrons that drift towards the anode of the TPC , which acts as readout. To attain a detectable signal, the primary electrons get amplified by a Micromegas structure. This structure consists of a woven wire mesh ($\sim 30\,\mu$m thick) and an anode plane, which are separated by a small gap [8]. When the primary electrons pass through the micromesh holes, they trigger an avalanche inside the gap. This generates detectable signals in both the anode pixels and the mesh [41]. A conceptual design of the detector is shown in Fig. 12.

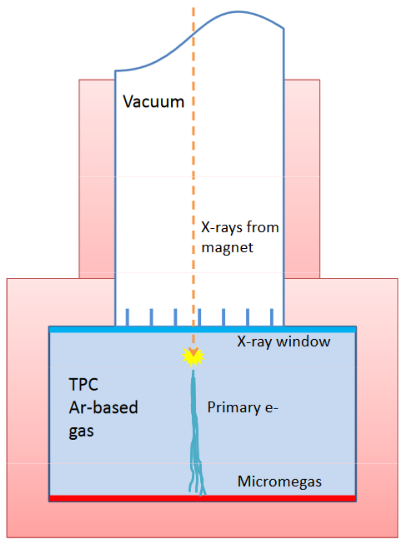

Figure 12: Conceptual design of a Micromegas X-ray detector. The X-ray photons originating from the magnet produce primary electrons inside the gas. These electrons drift towards the Micromegas structure, where they get amplified into a detectable signal. Adapted from [36].

3.4.4 Silicon Drift Detectors

Besides the Micromegas TPCs, various other detector systems have been proposed for the IAXO experiment. One of these detection systems are Silicon Drift Detectors (SDDs) [42], which are also used in the scope of the TRISTAN project and in this thesis [43]. The TRISTAN project seeks to investigate keV-sterile neutrinos by measuring the entire β tritium spectrum using the KATRIN experiment. To resolve the expected kink-like spectral distortion, an energy resolution better than 300 ev at 10 keV for electrons is required [2]. This exceeds the majority of IAXO's requirements. The good energy resolution is mainly driven by combining a large sensitive area with a small readout anode that results in a small detector capacitance, hence a good resolution. Another advantage is their low leakage current, which allows them to be operated at room temperature [44].

SDDs are made of silicon that has a pair creation energy of $E_{\mathrm{pair}} = 3.65\,\mathrm{eV}$ at room temperature [45]. Due to this low pair creation energy, a large number of charge carriers are created, resulting in a high energy resolution [46]. The detector comprises two different implementations of doped silicon. Silicon doped with electron donating atoms is referred to as n-type, while doping with electron acceptors is known as p-type. When the free charged carriers of both materials come into contact, they recombine in a process known as depletion. The detector consists of a large volume of high-resistivity n^- silicon that is surrounded between two layers of p^+ material. The p^+ layer at the entrance window of the detector forms the back contact electrode. The opposite side is segmented into concentric drift rings with a small-sized n^+ anode at the center. A voltage is applied between the concentric drift rings, creating an electric field inside the n^- silicon leading to the anode [47]. Furthermore, a voltage U_{bias} is applied between the back contact electrode and the anode. As a result, a zone within the n^- silicon without free charges is formed, referred as the depletion zone. Furthermore, a voltage is applied between the concentric drift rings, creating an electric field inside the n^- silicon leading to the anode [47].

When an ionizing particle with an energy greater than E_{pair} enters the depletion zone, electrons from the valence band are excited and move into the conduction band. This leaves holes that act as free positive charges behind. The electrons follow the potential of the electric field and drift towards the anode, while the holes are removed by the p^+ electrodes [44]. The amount of measured charge at the anode is proportional to the energy of the ionizing particle. The detector anode features an integrated Junction gate Field-Effect Transistor (JFET) that serves as a first amplification stage of the signal. This reduces signal loss, allowing for comparably long connections between the SDD and readout ASIC of several centimeters. A conceptual design of a SDD is illustrated in Fig. 13.

The primary advantages of SDD over baseline TPCs are their high energy resolution in the region of interest ($0 - 10\,\mathrm{keV}$) and lack of an entrance window. A small $50\,\mathrm{nm}$ deadlayer also lowers the threshold for low-energy X-rays to $< 0.5\,\mathrm{keV}$ and results in a high X-ray detection efficiency of $> 95\%$ in the region of interest [48].

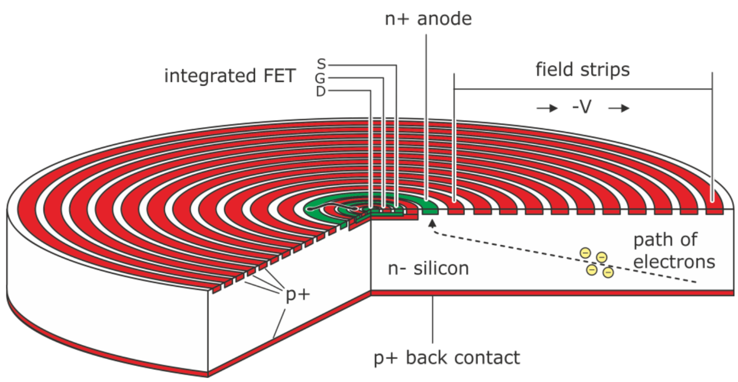

Figure 13: Conceptual design of a silicon drift detector. A bias voltage between the p^+ doped back contact and the n^+ doped anode (green) depletes the n^- silicon bulk. If an X-ray interacts inside this bulk, electron hole pairs are created. The electrons get guided by an electric field created by the p^+ doped drift rings to the anode. The integrated JFET is visible in the center of the SDD. Adapted from [44].

4 Experimental setup and procedure

The main objective objective of this work is to develop a first prototype detector board, which is essentially a printed circuit board (PCB) housing a TRISTAN SDD, alongside an Application-Specific Integrated Circuit (ASIC), in this case, ETTORE. The investigation was conducted in three stages:

1. Short PCB: The first stage was the proof of concept of house internal PCB production. In particular, it was verified whether the PCB design is functional and if the entire signal chain, including detector and readout electronics, works.

2. Long PCB: The second stage involved the testing of a PCB with the same design as the short PCB, with the only difference being a greater distance between SDD and readout ASIC. This distance was increased from 15 mm to 75 mm for this design. It was determined whether the long traces between the SDD and the readout ASIC are acceptable in terms of energy resolution since an increase of electronic noise is expected.

3. GIRAXO PCB: The last stage involved the test of a prototype PCB for a planned background demonstrator at the CanFranc underground low background laboratory. This PCB will be referred to as GIRAXO. The PCB designed and manufactured by the Milan-based company XGLab serves as the baseline for all comparisons.

The respective detector board is connected via flat ribbon cables to the detector bias system, whose outputs are connected via coaxial cables to a Data AcQuisition (DAQ) system CAEN DT5725. At the end of the signal line, a PC records the measured data. An overview of this signal chain is illustrated in Fig. 14. The following sections will describe each component in detail.

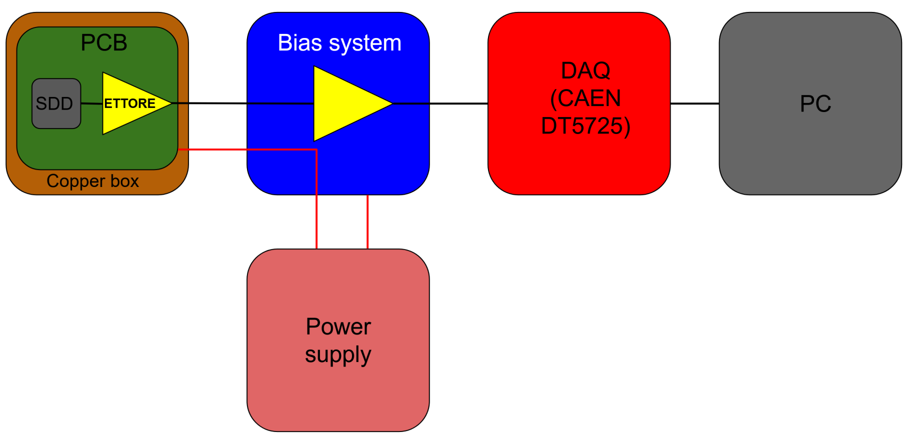

Figure 14: Overview of the read-out chain and experimental setup. The SDD is connected to an ETTORE readout ASIC. The ETTORE pre-amplifies the signal of the SDD. Both are mounted on a detector board, which is housed in a light-tight copper box. A connection to the bias system is established via flat ribbon cables, supplying the detector and ASIC with power through an external power supply. Additionally, the signal is buffered and amplified further before being routed to the CAEN DAQ, which digitizes the analog signal and prepares it for processing by a PC.

4.1 Detector boards

The detector boards developed in the scope of this thesis were all designed in KiCad, an Open Source Electronics Design Automation Suite (EDA) and strongly adhered to the design of the XGL-JFET-7CH-CARRIER board, which further serves as a baseline. The goal was develop a PCB design suitable for a background measurement at the CanFranc underground low background laboratory, where the signal-to-background ratio is critical to success. The idea was to increase the distance between the SDD and all of the readout electronics to reduce radioactive background close to the detector. During the course of this investigation, three different designs were created: Short, Long, and GIRAXO, all of which are four layer PCB designs made of FR-4 with an ENIG-RoHS surface finish. Design decisions concerning the GIRAXO PCB will be discussed in CH. 6.1. As illustrated in Fig. 15, the PCB consists of four copper layers.

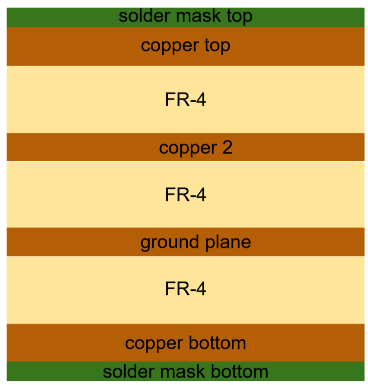

Figure 15: Layout of the PCB (cross section): the board consist of four copper layers and is made from FR-4 Standard Tg 130-140. The outer copper layers have a thickness of 35 μm, while the inner two are 17.5 μm thick. A ground plane is used to reduce parasitic coupling between signal lines belonging to different pixels. The total thickness of phase 1 PCBs is 1.6 mm and 0.8 mm for phase 2 PCBs.

All of the electronic components (ETTORE ASIC, capacitors, resistors), as well as the SDD are mounted on the copper top layer. The capacitors and resistors are Surface Mount Device (SMD) components that were soldered onto the PCB with the help of a reflow oven. A list of the components can be found in the appendix A.

The SDD used within the scope of this thesis were designed and manufactured by the Max Planck Society's Halbleiterlabor (HLL). They are 7-pixel SDDs with a pixel-diameter of 3 mm. The working principle of SDDs is discussed in Ch. 3.4.4. The drift rings of the detector are hexagonal in shape, allowing them to fill the entire detector area with almost gaps. Each pixel has its own integrated Junction gate Field-Effect Transistor (JFET) that is connected to its respective anode and serves as a first amplification stage of the signal. This reduces signal loss, allowing for comparably long connections between the SDD and readout ASIC of several centimeters. Figure 16 shows a photograph of a 7-pixel SDD and its connections to the PCB.

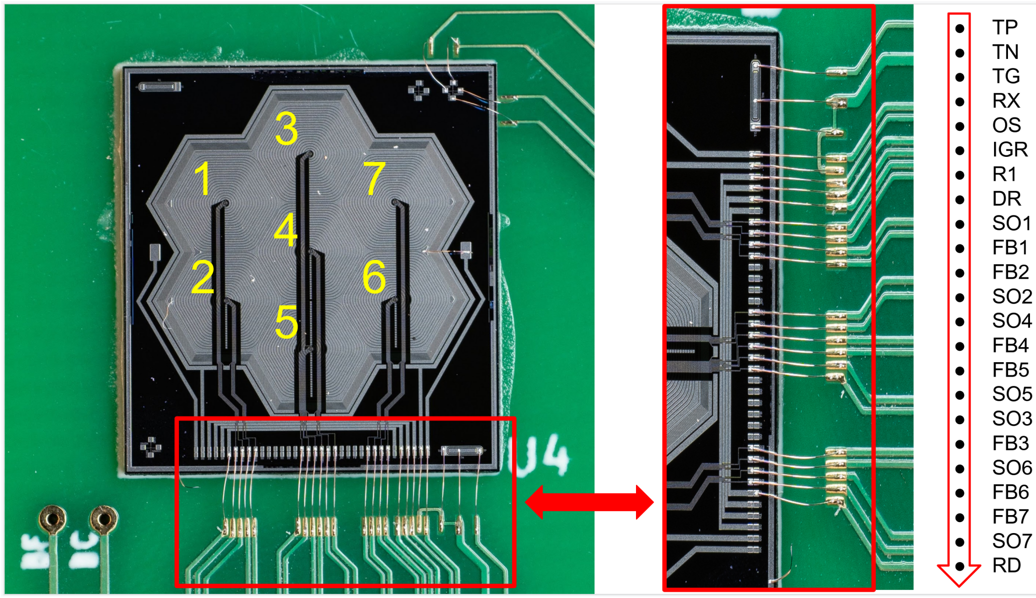

Figure 16: Photograph and pinout of the TRISTAN 3 mm 7-pixel SDD with integrated JFET. In yellow, the nomenclature of the pixels is given. The bonding between SDD and PCB is marked in red. This includes signal (SO1-SO7) lines and feedback lines (FB1-FB7) for each pixel and the power lines for every drift ring (R1, RX, IGR, RD, DR).

The SDD is glued non-conductively onto a 10 mm $\times$ 10 mm large cut-out. An electrical connection to the PCB is established via 25 μm thin bond wires. Figure 17 shows this process. Each bonding pad on the PCB has a parallel equivalent on the detector and is 100 μm $\times$ 500 μm in size. To ensure appropriate electrical connections, the bonding pads must be four times wider than the diameter of the bonding wire.

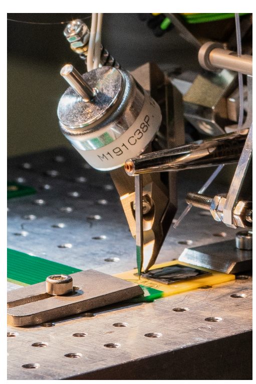

Figure 17: The bonding from SDD to PCB was performed by Danilo Mießner from HLL. A connection between the detector and the board was established by ultrasonically welding a 25 μm thin gold-aluminum wire to the corresponding pads.

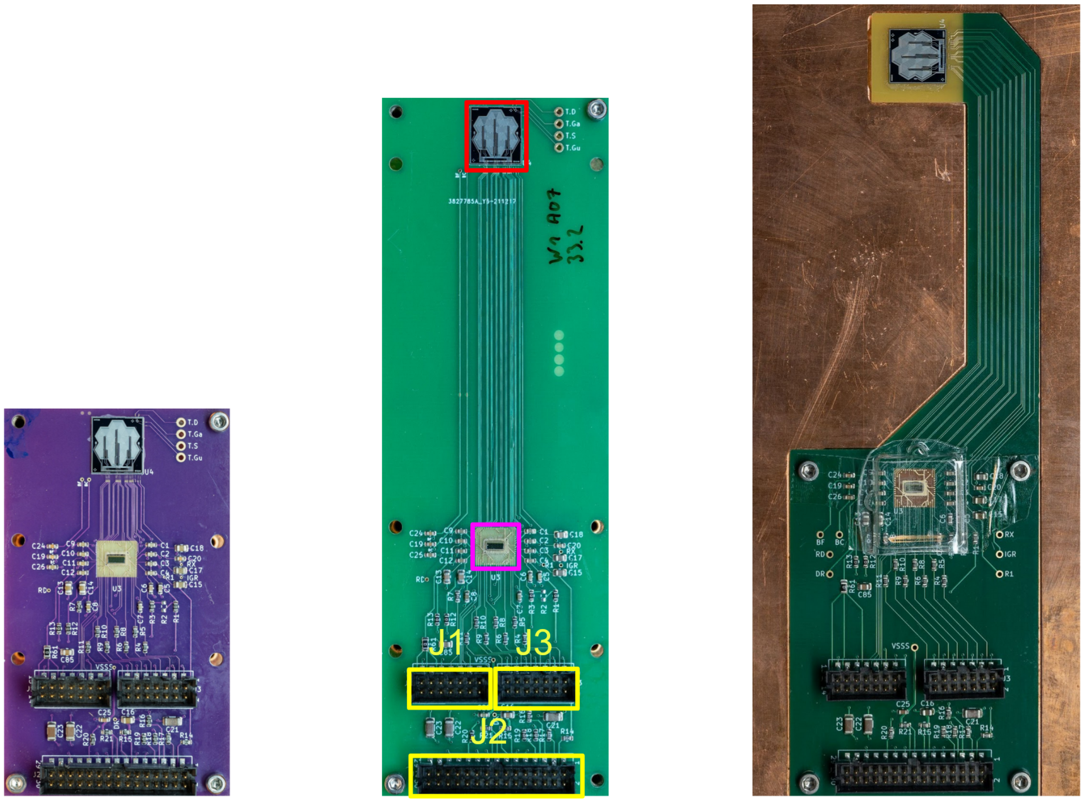

Figure 18: Top view of the Short, Long and GIRAXO PCBs. The SSD is indicated by the red box, the ETTORE ASIC by the magenta box. The distance between SDD and ASIC varies between the three PCBs and amounts to 15 mm for Short, 75 mm for Long, and 100 mm for GIRAXO PCB. The PCB is connected to the bias system via three connectors J1, J2 and J3 (yellow boxes).

All traces on the PCB leading away from the detector are 100 μm wide and are located on copper top, see Fig. 15. This excludes traces for Back Contact (BC) and Back Frame (BF), which are 250 μm wide and located on copper bottom. The reason for this is that the contacts for BC and BF are located on the side of the entrance window of the SDD. As a result, they bond to the detector on the other side. The BC voltage is responsible for providing the detector with $U_{\text{bias}} = -90\,\text{V}$, necessary for the depletion of the detector. The BF voltage with $U_{\text{bias}} = -100\,\text{V}$ prevents electrons near the detector's edge from leaving the sensitive area [47]. Both these traces, as well as the traces for supplying the voltages for the drift rings (R1, RX), are connected to the bias system via a connector denoted as J2, see Fig. 18. The drift ring voltages create a voltage gradient between $U_{\text{Ringx}} = -110\,\text{V}$ and $U_{\text{Ring1}} = -20\,\text{V}$ in the drift rings, guiding all electrons from the sensitive area to the anode in the center. All voltage supply traces are routed through various frequency-cutoff filters before being connected to the bias system. An example of such a filer is sketched in Fig. 19.

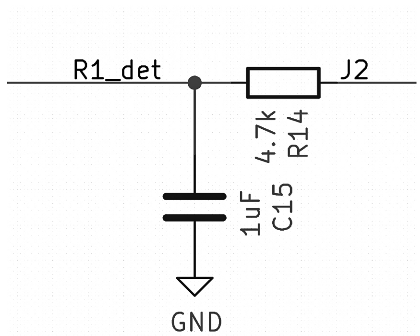

Figure 19: RC low pass filter for the R1 drift ring. The current flows from J2 to the bond pad R1 at the detector. The low pass filter consists of a capacitor and a resistor. It is designed to produce high attenuation above a specified frequency. This frequency is known as “cut-off” frequency.

Each pixel of the detector has its own signal and feedback line. The former are routed directly to the front-end inputs of the ASIC, while the latter are connected directly to the preamplifier outputs of the ETTORE. This signal loop is designed for a capacitive load up to 70 pF on both lines of each pixel (SO and FB). Exceeding this value raises the necessary current provided by the JFET and ETTORE’s first stage. As a result, the bandwidth of the feedback loop is reduced, which increases the signal rise time. This ’parasitic’ capacitance is the capacitance that originates from the signal line to ground. It is a major source of electromagnetic interference noise in electronic systems [49] and is caused by the potential difference created when current-carrying traces run close together. The capacitance increases with the trace length, therefore it should be more prevalent on the detector boards Long and GIRAXO. To reduce the parasitic coupling between signal lines belonging to different pixels, the traces have a distance of 100 μm.

ETTORE is a multichannel ASIC designed to read out SDDs with an integrated JFET and is produced by XGLab. It has twelve channels, seven of which are used. All channels consist of a preamplifier, an AC-coupled second amplification stage, and a comparator designed to detect preamplifier saturation. It is possible to select between the two amplification stages when acquiring data. The selection can be done by providing a digital signal to a dedicated pad (SELECT-PRE). A representation of this circuit is visible in Fig. 20.
In the first stage, the output signal is superimposed on a linearly increasing ramp, while in the second stage, it appears as a steeply rising pulse followed by an exponentially decaying tail. Waveform examples of both stages are shown in Fig. 20 in blue. The visible ramps represent a continuous increase in the waveforms caused by a constant detector leakage current. When a particle interacts in the detector, many electron hole pairs are created, increasing the output voltage. Such an event causes a sharp step in the waveform, with the height of the step corresponding to the amount of charge created in the event. To avoid a saturation of the readout ASIC, a reset is performed at a predetermined threshold, i.e. positive voltage is applied to the detector discharge diode. This operation is performed only on the detector and results in a sharp decrease in the waveform. The duration of the reset ranges between 300 ns and 2 μs. During the reset, the ETTORE receives a digital inhibit signal, which ensures that the second stage output remains consistent [50].

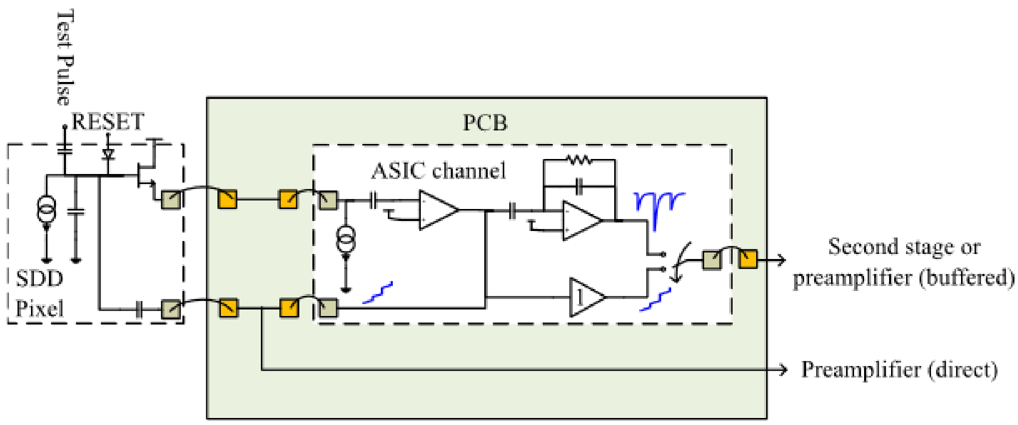

Figure 20: Output selection of the ETTORE ASIC. Following pre-amplification, ETTORE offers two signal modes: direct output from the preamplifier or an AC coupled, buffered output signal. Waveform examples are shown in blue. Adapted from internal ETTORE report, April 29, 2020

Each ETTORE channel has a single output and a corresponding connection to ground, both of which are routed to the connector J3. There, a connection with the bias system is established. The ETTORE is glued conductively on a solder mask-free copper plane that is connected to the ground plane with vias, see Fig. 21. The ETTORE is surrounded by 56 pads spaced 175 μm apart on four sides and is connected to the PCB by thin bonding wires.

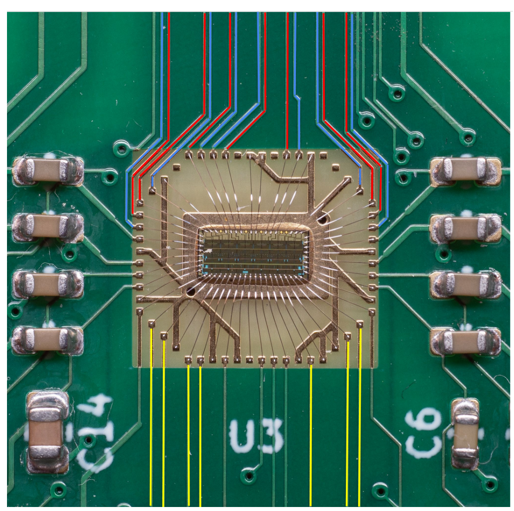

Figure 21: The ETTORE ASIC is mounted on a copper plane and is bonded to 56 pads. The blue traces represent signal lines from the SDD to the front-end inputs of the ETTORE. The feedback lines (red) connect the ETTORE's preamplifier outputs to the SDD. The yellow traces constitute the ETTORE output lines, that link up to the bias system.

4.2 Detector calibration with ^{55}Fe

To compare the performance of Short, Long and GIRAXO PCB the spectrum of a radioactive ^{55}Fe source was for each recorded, since it provides x-ray lines in the keV-region of interest for IAXO. The isotope ^{55}Fe decays to ^{55}Mn with a half-life of 2.737 years via electron capture [51]. Since an electron from a higher-lying shell fills the vacancy in the K shell, an Auger electron with an energy of 5.19 keV is emitted. In addition, three X-rays are emitted: MnKα_1 at 5.89875 keV, MnKα_2 at 5.88765 keV, and MnKβ at about 6.49 keV [52]. The first two lines cannot be distinguished due to their small distance and are approximated with the line MnKα at 5.89 keV. The calibration of the SDD is performed with the MnKα and MnKβ X-ray lines, which is required since the internal unit of the DAQ is in ADC. The calibration using only these two lines is feasible since the TRISTAN detectors have an excellent ADC linearity over a wide energy range of 10 keV to 60 keV, deviating only by $< 0.1\,\%$ [2]. Both lines also make it possible to compute the energy resolution of the detector. During the measurements, the ^{55}Fe source was placed at a distance of about 3 cm below the detector for phase 1 PCBs and 6 cm for phase 2 PCBs.

4.3 Bias system

A bias system developed by the company XGLab was used for the measurements carried out in the scope of this thesis this thesis. It is used to operate the SDD and the ETTORE ASIC on the detector board and is itself biased with 25 V and 1.5 A through an external power supply. Figure 22 shows a photograph of the bias system, which consists of a buffer board mounted on a control board. The latter is connected to the detector board via the 30 pin connectors J3 and J5, which supply voltages to the ETTORE ASIC and the drift rings of the SDD, while the buffer board connects via J8, buffering and amplifying the outputs of ETTORE. An on-board pulse generator on the control board provides a 2 ms periodic reset, keeping all pixels of the SDD synchronized. Through the outputs Out0-Out6 a connection via coaxial cables to the DAQ system is enabled.

4.4 Data acquisition system

For the measurements carried out in this thesis, the CAEN DT5725 was used for data acquisition, see Fig. 23. It is an eight channel digitizer with a sampling rate of 250 MS/s and a 14-bit resolution. Furthermore, it features a Digital Pulse Processor (DPP) allowing for Pulse Height Analysis (DPP-PHA) and Pulse Shape Discrimination (DPP-PSD). The acquisition is fully controlled by the CoMPASS software, which manages the DPP algorithm parameters and saves the relevant energy, time, and PSD spectra. The settings used for data acquisition can be found in the appendix B. To prevent read-out during a reset, the inhibit signal from the SDD's amplifier is routed through the bias system and fed into the TRG IN port of the CAEN digitizer. The DAQ was operated in waveform mode, meaning that all waveforms were saved individually. Every waveform was recorded with a trace length of 20 μs and a pre-trigger time of 4 μs. The waveforms that are saved are chosen using a digital leading edge trigger algorithm. The algorithm detects events when one of its samples exceeds a predefined threshold value. For each channel, the waveforms are saved independently for offline waveform processing.

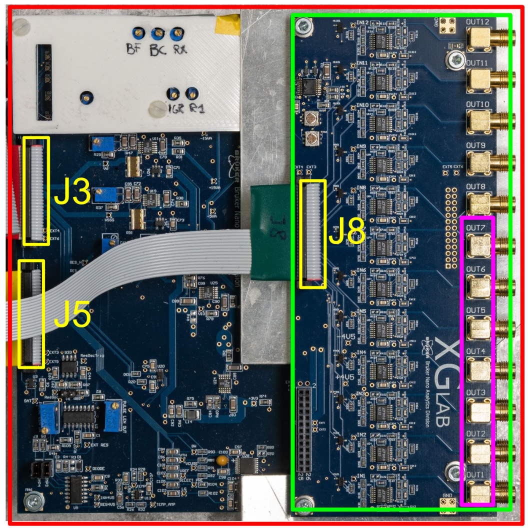

Figure 22: The XGLab bias system comprises a buffer board (green) mounted on top of the control board (red). The system provides the supply voltages for the detector, reset logic, and buffering and amplification of incoming signals. It is connected via the connectors J3, J5 and J8 (yellow) to the detector board and via Out0-Out6 (magenta) to the DAQ system.

Figure 23: The CAEN DT5725 is a 14-bit digitizer with a sampling rate of 250 MS/s. The raw waveforms for each channel were saved separately. Adapted from the manual.

5 Data Analysis

5.1 Data Analysis Procedures

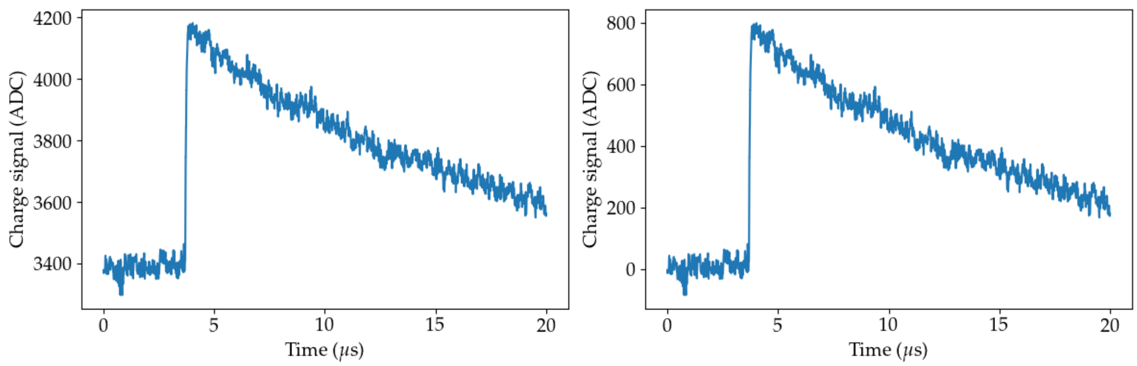

(a) Uncorrected waveform.

(b) Baseline-corrected waveform.

Figure 24: Example for the baseline correction of a waveform. (a) The first 625 samples of a raw waveform are averaged. (b) The baseline mean is then subtracted, yielding a baseline-corrected waveform.

The analysis is based on individually recorded second stage waveforms. Each waveform contains 5000 samples recorded at a sampling rate of 250 MS/s, corresponding to a trace length of 20 μs. The height of the waveform is given in ADC units. An example is shown in Fig. 24 (a). All signal processing, shaping, and parameter extraction is performed using offline algorithms developed for the characterization of germanium detectors [53].

Baseline restoration

Since the waveforms were measured with an internal ADC offset, one has to correct for it. For this purpose, the first 625 baseline samples (2.5 μs) of a waveform are averaged. This average value is then subtracted from each sample, yielding a baseline-corrected waveform, as shown in Fig. 24 (b).

For subsequent analysis, the baseline-corrected waveforms are used. In addition to the baseline-mean, the baseline root mean square (RMS) is determined. The baseline RMS is used to estimate the electronic noise. It is the standard deviation of the first 625 samples of a waveform.

Pole-zero correction

Driven by the architecture of the readout electronics, each signal features an exponential decay with a theoretical decay time of 15 μs. Consequently, a pole-zero correction is applied to these waveforms to obtain step-like waveforms. The decay time τ of the system must be determined in order to perform the pole-zero correction. To obtain the precise value of τ, the individual decay times of each signal are extracted. The tail is modeled using the function

$$y(t) = A\exp(-t/\tau), \tag{13}$$

where A denotes the amplitude and t the time. From this, the decay time τ can be extracted by fitting a linear function to the logarithm of y(t). The fit range is constraint to $14\,\mu s \leq t \leq 20\,\mu s$. For each pixel of the detector the decay times of all waveforms are histogrammed to obtain the decay time distribution, see Fig. 25.

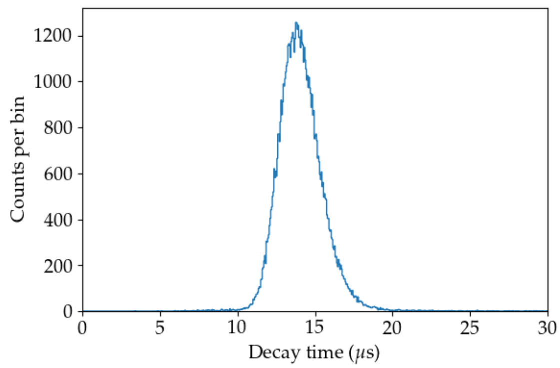

Figure 25: Example of a decay time distribution. The decay times of all events are determined and then histogrammed. For the pole-zero correction, the distribution's peak position is determined.

The distribution can be modeled using the Lorentzian function which is given by

$$f(x) = A\left(\frac{\gamma^2}{(x - x_0)^2 + \gamma^2}\right), \tag{14}$$

where A denotes the amplitude, γ the half width at half maximum and x_0 the peak position. During this investigation, the obtained value of x_0 is $\sim 13\,\mu s$. This value is then used as the decay time for the pole-zero correction of each waveform. For this purpose, the waveform is processed with an infinite response filter of the form:

$$y(t) = y[t\text{-}1] + x[t] - \exp(-1/\tau)\cdot x[t\text{-}1], \tag{15}$$

where y[t] describes the deconvolution of the signal x[t] at time t. The resulting waveform has a step-like form, see Fig. 26.

Pile-up rejection

Different quality cuts are applied to the pole-zero corrected waveforms, including pile-up rejection. Pile-up is the superposition of two events. This can happen pre-trace, when the baseline combines with the exponential tail of the previous event, or in-trace, when two events combine within the same trace. The slope of the baseline can be used to identify pre-trace pile-up events. To determine it, a linear function is fitted to the first 625 samples of a waveform. If the baseline-slope exceeds a certain threshold, the event is rejected. An in-trace pile-up is identified with the help of a fast

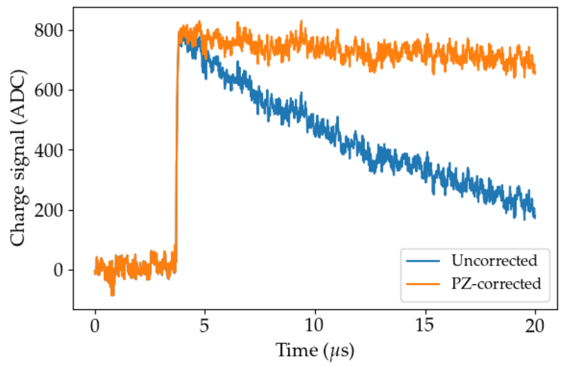

Figure 26: Example of a pole-zero correction. The baseline-corrected waveform (blue) is deconvolved from its exponentially decaying tail, resulting in a pole-zero corrected waveform (orange).

trapezoidal filter with a rise and fall time of $0.2\,\mu$s and a flat top of $1\,\mu$s. If the shaped signal of the trapezoidal filter exceeds the threshold of twice the baseline RMS for a duration longer than the flat top, an energy deposition is identified. If the number of energy depositions within one trace exceeds one, the event is rejected. An example of a in-trace pile-up event is depicted in Fig. 27.

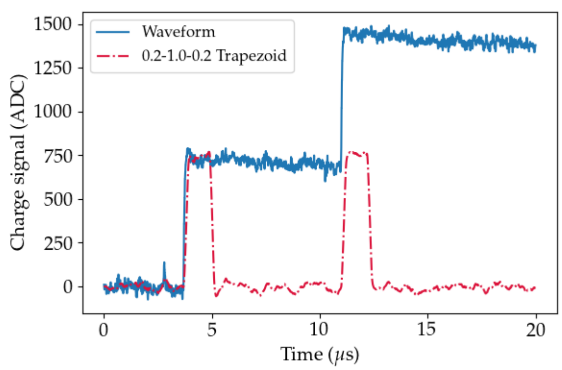

Figure 27: In-trace pile-up events are identified by using a trapezoidal filter, which is used to determine the number of energy depositions within the trace length of $20\,\mu$s. The waveform is rejected if this number is greater than one.

Energy reconstruction

The energies of the events were reconstructed using an adjustable trapezoidal filter applied to the pole-zero corrected waveforms. For the data analysis of Short and Long the flat top time of the filter was kept at $0.2\,\mu$s and for GIRAXO at $0.5\,\mu$s. The filter rise time was moved between $0.2\,\mu$s and $4\,\mu$s, resulting in ten different filters. Therefore, ten energy values are saved for each waveform. Finally, the energy is extracted from the shaped signal at the center of the flat top region, see Fig. 28. This is preferable to a pick-off at the maximum, which would result in a bias towards higher values due to noise fluctuations.

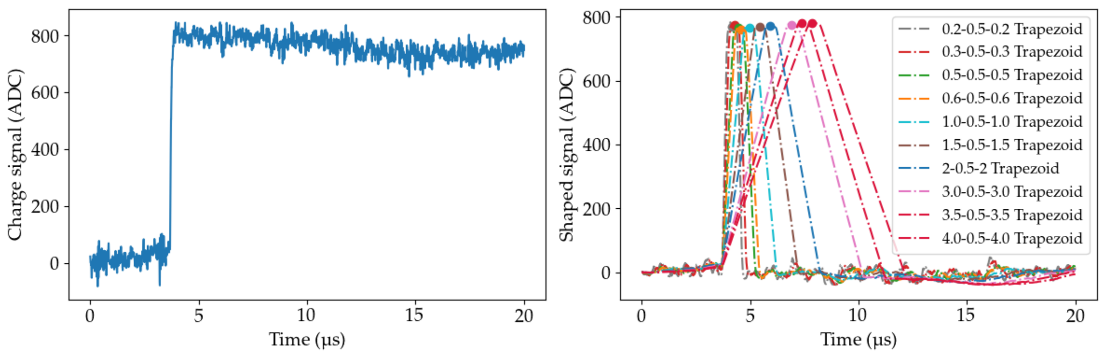

(a) Charge signal.

(b) Shaped charge signal (trapezoid).

Figure 28: Example for the reconstruction of the energy of an event. A trapezoidal filter is used to process the pole-zero-corrected waveform (a). The energy is then extracted from the shaped signal (b) at the flat top's center, denoted by a point. This procedure is repeated for ten distinct filter rise times (0.2, 0.3, 0.5, 0.6, 1.0, 1.5, 2.0, 3.0, 3.5, 4.0) μs.

Signal rise time computation

The signal rise time is extracted as the time taken by a signal to change from 10% to 90% of the maximum amplitude of the leading edge. Before computing the rise times of the individual events, waveform smoothing is performed to reduce noise. A Savitzky-Golay filter is used for this purpose. This filters works by fitting a low-degree polynomial

$$p(n) = \sum_{k=0}^{n} a_k n^k \tag{16}$$

to a sequence of samples by the method of least squares. By evaluating $p(n)$ at the central point of the sequence $n = 0$, the smoothed output value is obtained. Effectively, the output value is the 0th polynomial coefficient [54]. The filter was applied to the pole-zero corrected waveforms multiple times before extracting the signal rise time, see Fig. 29.

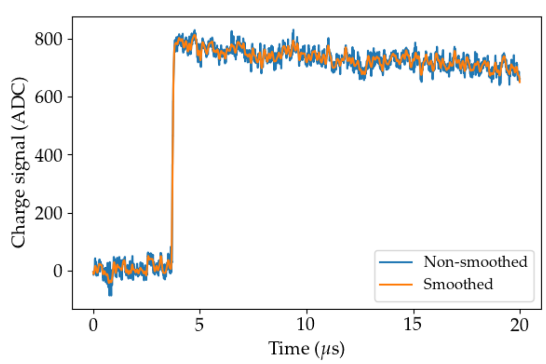

Figure 29: Example of waveform smoothing with a Savitzky-Golay filter.

For the determination of the signal rise time, the smoothed waveform is first divided by the maximum pulse height. The rise time is then defined as the difference between the times that correspond to 90% and 10% of the maximum amplitude. Both values are obtained by moving backwards and forwards from the time corresponding to 50%. Furthermore, interpolation between the relevant samples was used to increase precision. An example of the entire procedure can be found in Fig. 30.

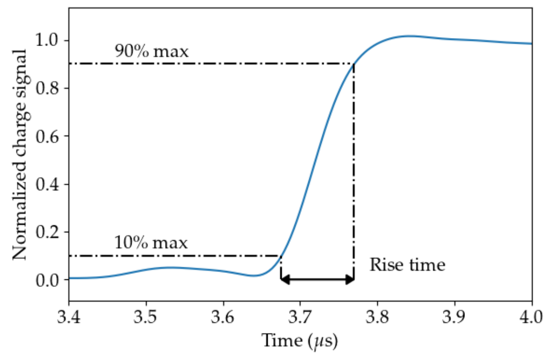

Figure 30: Example for the signal rise time computation. The rise time is obtained from the normalized and smoothed waveform.

Energy calibration and resolution computation

After collecting the individual energies of events into a histogram, a peak-search algorithm is used to find the MnKα and MnKβ lines in ADC values. Both peaks are fitted with a Gaussian of the form

$$f(x) = A \exp\left(-\frac{1}{2}\frac{(x-\mu)^2}{\sigma^2}\right) \tag{17}$$

to achieve greater precision in their ADC position. Here, σ denotes the standard deviation and μ the mean, which is used as the position of the peaks. Knowing that the MnKα and MnKβ lines have energies of 5.89 keV and 6.49 keV, respectively, allows one to relate the energies in ADC with the energies in keV. This is accomplished by plotting the keV energies over the ADC energies and then fitting the plot with a linear function that will serve as the calibration curve. An example for the calibration can be seen in Fig. 31.

The calibration curve is applied to each spectrum, resulting in spectra with energies in keV. These calibrated energy spectra are used to calculate the FWHM. For this purpose the data is fitted with a function of the form

$$\begin{aligned} f(E) = &\frac{A}{\sqrt{2\pi}\sigma_1}\exp\left(-\frac{(E-\mu_1)^2}{2\sigma_1^2}\right) + \frac{B}{2}\left(\mathrm{erf}\left(-\frac{(E-\mu_1)}{\sigma_1}\right)+1\right) \\ &+\frac{C}{\sqrt{2\pi}\sigma_2}\exp\left(-\frac{(E-\mu_2)^2}{2\sigma_2^2}\right) + \frac{D}{2}\left(\mathrm{erf}\left(-\frac{(E-\mu_2)}{\sigma_2}\right)+1\right). \end{aligned} \tag{18}$$

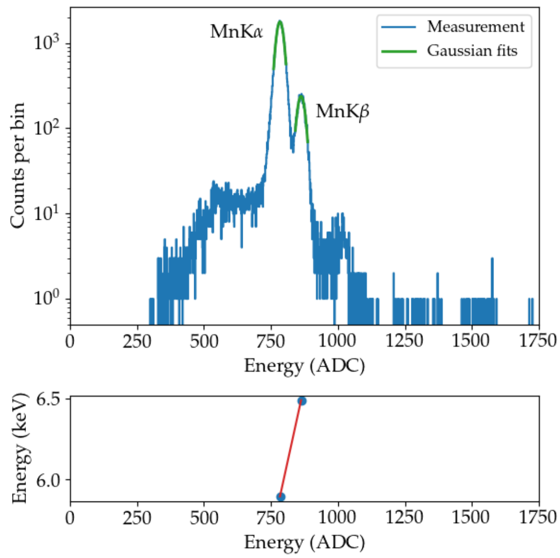

Figure 31: Example for an energy calibration. The upper plot shows an uncalibrated ^{55}Fe spectrum. By fitting Gaussians to the peaks, it is possible to extract the position of the MnKα and MnKβ lines. The calibration curve (lower plot) is derived by relating the true (keV) and obtained (ADC) energies with a linear function.

The first line of terms in this equation describes the MnKα peak, while the second line describes the MnKβ peak. Each peak is approximated by a Gaussian function and a Gaussian error function. The latter is a low-energy tail of the peak, which accounts for the fact, that not all energy is deposited in the detector [2]. Furthermore, A, B, C and D describe the amplitudes of the respective functions, while the factor $1/(\sqrt{2\pi}\sigma_i)$ ensures normalization to the area [55]. The FWHM is then calculated from the MnKα peak, which is described by the fitted function's first peak. Fig. 32 shows an example of the FWHM extraction.

This procedure was repeated for various shaping times. The optimal resolution for Short and Long was obtained for $rt = 2.0\,\mu$s and $ft = 0.2\,$ns, while for GIRAXO it was obtained for $rt = 2.0\,\mu$s and $ft = 0.5\,$ns. These values are used for the subsequent comparison.

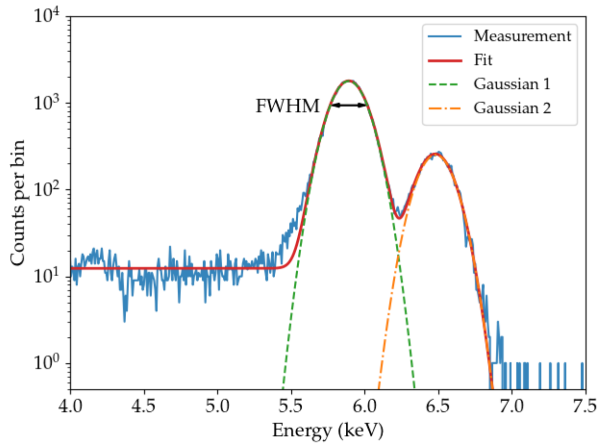

Figure 32: The calibrated ^{55}Fe spectrum is fitted with the function in Eq. 18, which is highlighted in red. The green and orange lines represent the Gaussian parts of the two peaks, respectively. The FWHM is calculated from the fit function's MnKα peak.

5.2 ^{55}Fe energy spectrum of the detector boards

In a first step, the uncalibrated energy spectra of the different boards are compared to each other. A histogram containing the energies of all seven pixels is generated for each detector board. The three obtained histograms are plotted on top of each other in Fig. 33 (a). In all three histograms the MnKα and MnKβ lines are visible and separated.

The plot clearly shows that GIRAXO's energy spectrum slightly differs (shifted and compressed) from the other boards. This shift amounts to about 100 adc units and is caused by a decrease in gain for the GIRAXO PCB. The reduced gain may be attributable to the distance between the SDD and the ASIC, as longer distances result in higher parasitic capacitance, requiring higher currents to drive the signal lines, or to differences in the specific ASIC used on the GIRAXO PCB. This distance is 15 mm for Short, 75 mm for Long, and 100 mm for GIRAXO. Adjusting the voltages on the ETTORE ASIC may cause the gain of the individual boards to change. Furthermore, there is an energy threshold at about 300 adc in all three histograms, which results in a higher threshold in terms of keV for the low-gain GIRAXO board. The threshold is unaffected by the trigger threshold setting, as different values were utilized for the measurements, see Appendix B. The origin of the threshold will be investigated beyond the scope of this thesis. The calibrated spectra of Short, Long, and GIRAXO are shown in Fig. 33 (b). The energy threshold for Short and Long is ≈ 2.4 keV, and for GIRAXO it is ≈ 3 keV. A further noticeable observation is the number of events. While the MnKα peak of Short and Long has ≈ 12500 counts, GIRAXO's has only ≈ 2600 counts. Both values were obtained with a total measurement time of 5 minutes. The discrepancy originates from the difference in the positioning of the ^{55}Fe source. The SDD receives x-rays emitted by ^{55}Fe source according to the inverse-square law. Since the GIRAXO board was placed approximately twice as far from the ^{55}Fe source as Long and Short, one expects a four times lower number of events. This seems to be consistent with the measurements.

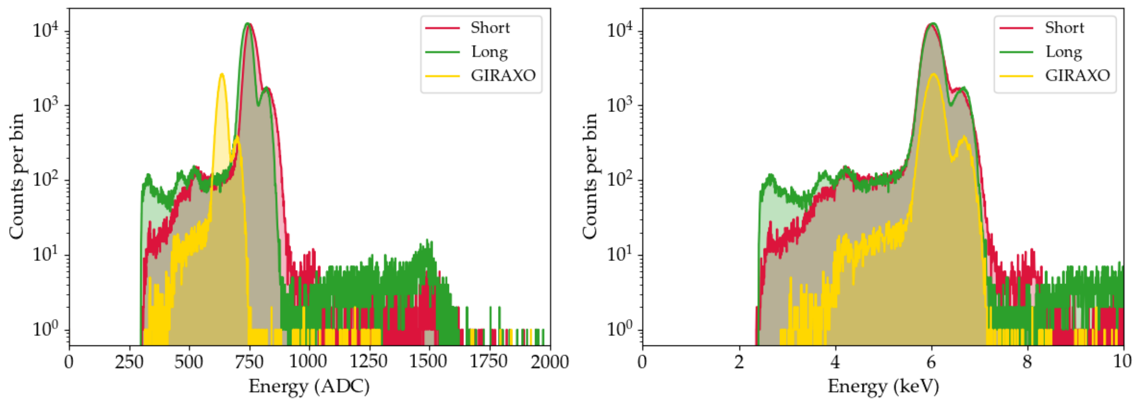

(a) Uncalibrated spectra.

(b) Calibrated spectra.

Figure 33: (a) Uncalibrated energy spectra of ^{55}Fe recorded with Short (red), Long (green) and GIRAXO (yellow) at room temperature. (b) Calibrated energy spectra with an energy resolution of 260 ± 11 eV, 261 ± 9 eV and 269 ± 9 eV (FWHM) at 5.9 keV, respectively. In all spectra the MnKα and MnKβ peaks appear separated.

For Short and Long it is possible to observe the silicon escape peak at 4.2 keV. The escape peak originates from the fact that there is a 4.3% chance that a fluorescence photon with an energy of 1.7 keV will be emitted if a photon with an energy greater than the silicon K edge (1.8 keV) is absorbed inside the silicon [56]. If the energy of the fluorescence photon is not deposited inside the detector active volume, an escape event with an energy of $E_{\text{escape}} = E_{\text{MnK}\alpha} - 1.739\,\text{keV}$ is measured. For GIRAXO this peak is only slightly visible due to reduced statistics.

To compare the performance of the individual detector boards' pixels, their spectra are combined into single plots, as shown in Fig. 34. A nomenclature of the detector's pixel was given in Fig. 16. As can be seen in the plots, the different pixels appear to be consistent, with no obvious outliers.

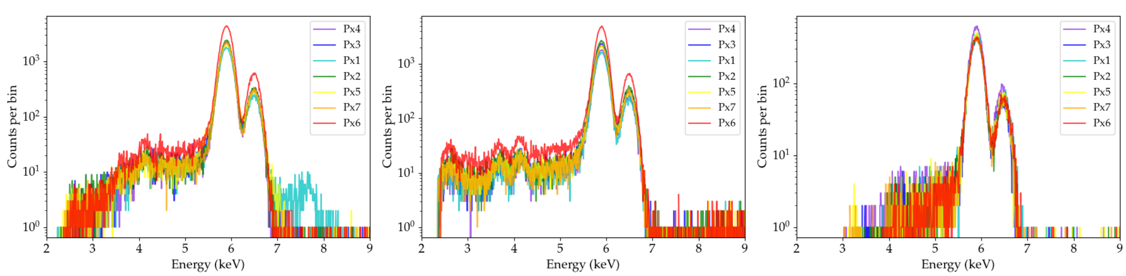

(a) Short

(b) Long

(c) GIRAXO

Figure 34: Calibrated ^{55}Fe spectra of individual pixels recorded at room temperature with Short (a), Long (b) and GIRAXO (c).

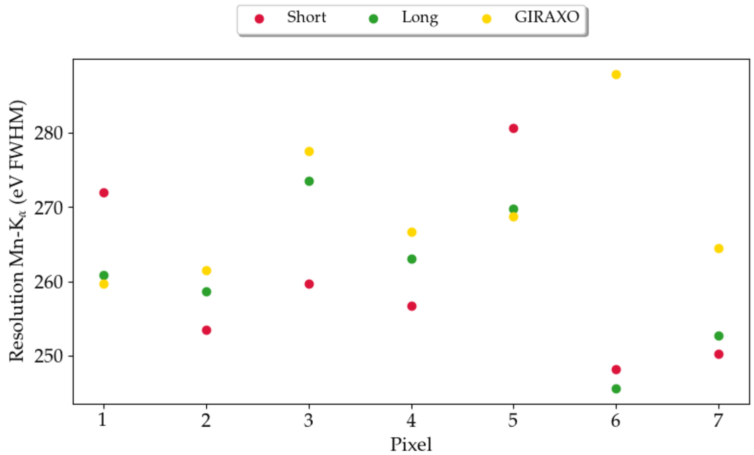

Figure 35: Comparison of obtained values for the Full width at Half Maximum (FWHM) of the individual PCBs pixels. All three PCBs provide the necessary energy resolution. Furthermore, the pixels of Short and Long seem to follow the same trend except which is not the case for GIRAXO.

Using the procedures of Ch. 5.1, the FWHM is computed for each pixel of each detector board. The results are summarized in Fig. 35.

All of the FWHMs in the plot are less than 300 eV, which is sufficient for the IAXO purpose. Using the data from the plot, one can compute the mean values and standard deviations for the FWHMs for each PCB, in order to compare their overall performance. For Short, Long and GIRAXO an energy resolution of (260 ± 11) eV, (261 ± 9) eV and (269 ± 9) eV, respectively, is achieved. No significant degradation of the energy resolution with increasing distance between detector and ASIC is observed. Furthermore, the performance of individual pixels is consistent, with only minor deviations, such as pixel 6 of GIRAXO, which has a FWHM of 288 eV. At this point, it should be noted that the resulting FWHM is highly dependent on the initial fit range of the X-ray peaks.

5.3 Signal rise time distributions

As stated in Ch. 5.1, the signal rise time of an event is estimated as the time it takes a signal to change from 10% to 90% of the maximum amplitude of the leading edge. It is a crucial timing property of the detector board and especially important for experiments with a high count rate, such as TRISTAN. A high count rate is not required for IAXO. This is in particular true since the time component of the signal does not contain the decisive parameter—the energy of the interacting particle. The signal rise time depends on the SDD's response time as well as the capacitive load on the signal loop between SDD and ASIC. The former arises because of the collection time for electrons and holes within the semi-conductor, which varies depending on the location of the ionizations in regards to the collecting anode [46]. The signal rise times of the detector boards are plotted for each pixel, as shown in Fig 36.

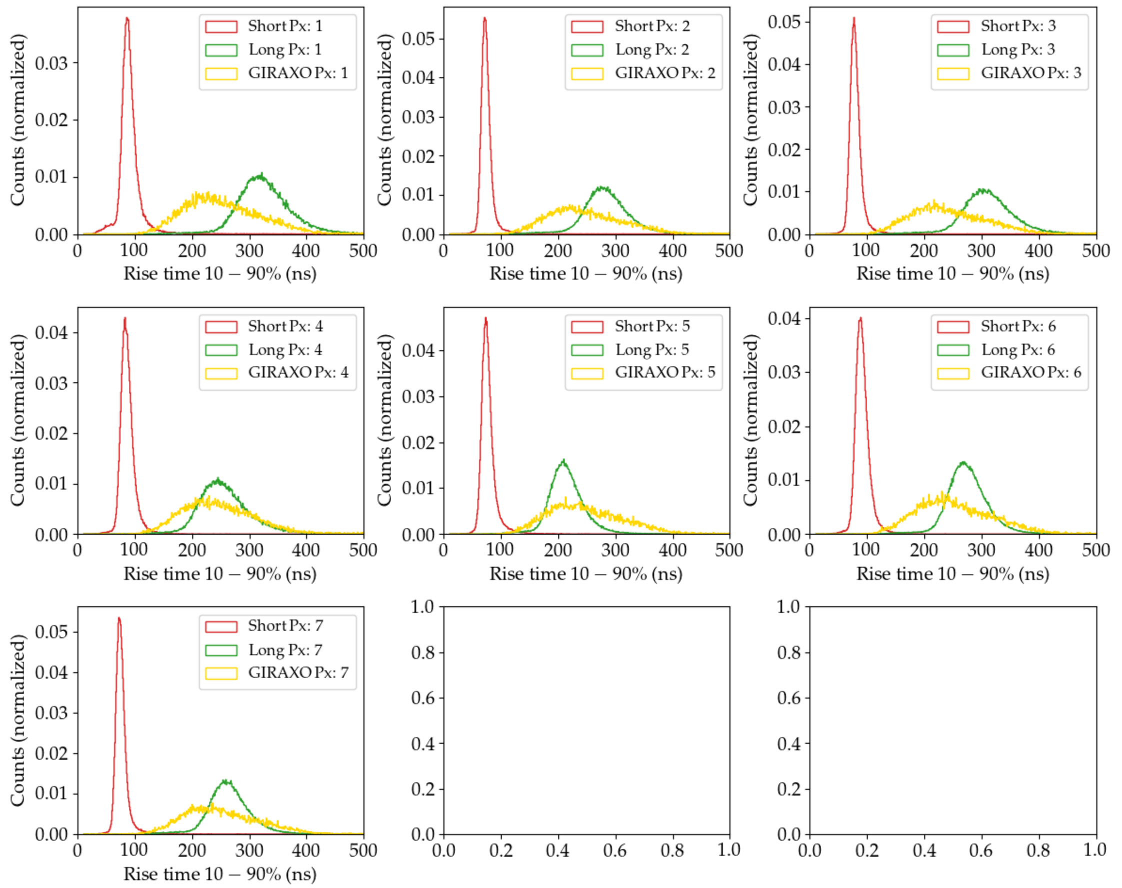

Figure 36: Signal rise time distributions (SRTDs) for Short (red), Long (green), and GIRAXO (yellow). Shorts has the narrowest SRTDs with the shortest mean rise times. GIRAXO performs better than Long with lower rise times, but has the highest variance. Long's pixels appear inconsistent, with a wide range of mean values.

The signal rise time distributions (SRTDs) are distributions, with varying expectation value and width. General statements can be made that apply to a particular board. As expected, Short has the best performance, characterized by SRTDs with low mean and width, which also appear consistent through the pixels. Long and GIRAXO are expected to perform worse due to longer traces that introduce additional capacitive load. Despite having longer traces, the SRTDs of GIRAXO have a lower mean than Long. This could be due to the use of fewer vias within the signal loop of GIRAXO, which induce parasitic capacitance. Furthermore, the plots clearly show an increasing SRTD-width with increasing signal line trace length. Using the data of the histograms, the values of the median and mean of each pixel can be obtained, see Fig. 37.

The plot confirms the findings obtained from the SRTDs by demonstrating that the separation between SDD and ASIC has a significant impact on the mean rise time values. An overall mean rise time of (83 ± 6) ns, (276 ± 34) ns and (251 ± 3) ns for Short, Long, and GIRAXO is computed

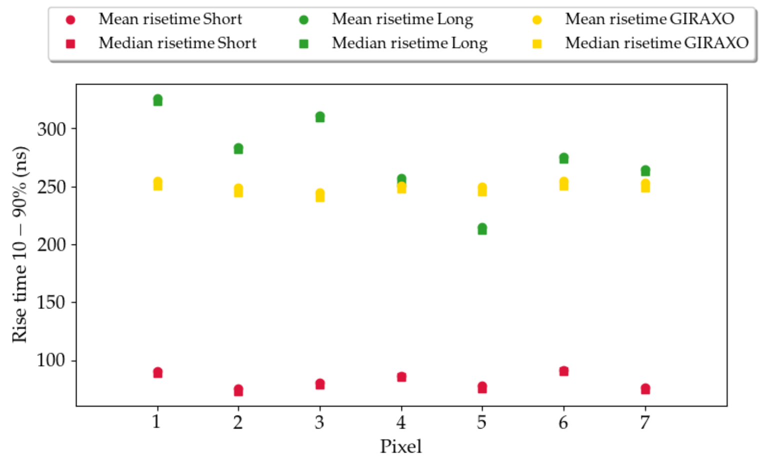

Figure 37: Comparison of mean and median rise times of Short, Long and GIRAXO. Clearly Short has the shortest signal rise times with a mean of $83 \pm 6\,\mathrm{ns}$. Long has the longest rise times and sees the biggest spread of means with $276 \pm 34\,\mathrm{ns}$. GIRAXO has a mean of $(251 \pm 3)\,\mathrm{ns}$, which is sufficient for IAXO.

using the data from the plot. The error is estimated as the standard deviation around the mean. Furthermore, the success of minimizing the induced capacitance in phase 2 PCBs can be deduced from the findings. This is suggested by the fact that, despite having longer signal lines, GIRAXO performed better than Long.

5.4 Noise components

Noise is defined as disturbances in the signal that impede the ability to distinguish between signal structures and therefore reduce the resolution. There is a distinction to be made between signal fluctuations and electronic noise, which are inherent to a system, and electromagnetic interference, which is induced externally, such as from power supplies or common grounding. The signal fluctuations arise in the silicon chip, whereas the dominant electronic noise of a system is a feature of the read-out electronics. Furthermore, the shaping times of the energy filter, which define the susceptibility to distinct frequencies, are essential.

Fano limit

Even with all noise sources eliminated, there is an unavoidable limit of resolution, the Fano limit. This limit is a signal fluctuation that arises from the fact that the number of ion pairs created inside the semi-conductor fluctuates. It applies to any process in which an energy is converted to an electric charge. The broadening of the Gaussian peaks in the spectrum due to Fano noise can be described by

$$\sigma^2 = FJ. \tag{19}$$

The Fano factor, which is an intrinsic constant of the detecting medium, is denoted by F, and the mean produced ionization due to an event is expressed by J. The Fano limit for SDD at the

MnKα peak's energy (5.9 keV) is $\Delta E_{\text{Fano}} = 119\,\text{eV}$ (FWHM) [43]. This is the theoretical limit of the achievable resolution.

Thermal noise

Thermal noise is a type of electronic noise that can be found in any conductor or semi-conductor and is caused by the thermal Brownian motion of charge carriers. This thermal motion causes velocity fluctuations in the current flow inside resistors and is independent of the flowing current [57]. The resulting fluctuations have a a high frequency. As a result, a longer filter rise time allows one to average out these fluctuations. The amount of thermal noise contribution decreases as the filter rise time increases and increases as the capacitance C decreases [43].

Shot noise

Shot noise is a form of electronic noise that can be described as a statistical fluctuation of charge carriers that occurs when charge carriers cross potential barriers, such as pn-junctions. It exists because electric current is composed of quantized packets whose movement is governed by uncertainties. The amount of shot noise is proportional to the SDD's leakage current and is thus also known as current noise [57]. When using longer filter rise times, the filter becomes susceptible to changes in the leakage current. Therefore, the shot noise increases with filter rise time [43].

1/f noise

In a more general sense, 1/f noise refers to all noise contributions that exhibit a 'non-white' frequency response and is also known as pink noise. Its origins are not yet fully understood since there exists an ambiguity as to whether it is a fundamental statistical consequence or a property of specific systems [57]. There are models that explain it through fluctuations in the number of free carriers due to generation-recombination within JFETs and MOSFETS [58]. The amount 1/f noise increases with capacitance coupled to the signal loop and remains constant regarding the filter rise time [43].

Taking all noise contributions into account one can model a theoretical noise curve, see Fig. 38 The amount of noise is characterized by the unit equivalent noise charge (ENC).

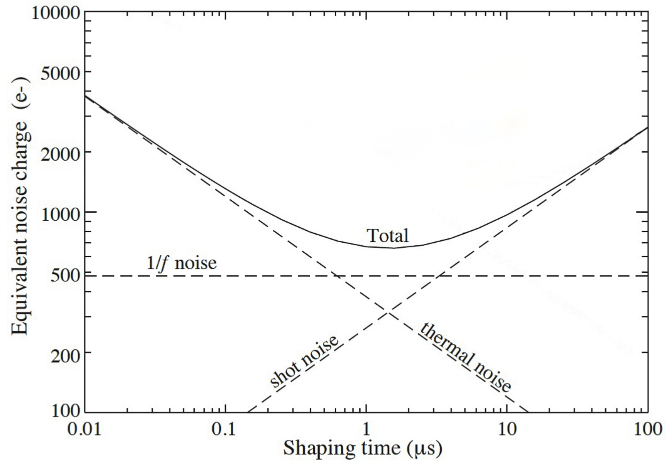

Figure 38: The theoretical noise curve is the total of all noise contributions. As the filter rise time increases, the contribution of shot noise increases while the contribution of thermal noise decreases. The contribution of 1/f noise can be seen as constant. The optimal filter rise time is the minima of the total noise curve. Adapted from [57].

5.5 Noise quantification

The noise of the three detector boards is compared in this section. This includes a comparison of the baseline root mean square (RMS) and noise curves.

5.5.1 Baseline RMS

The baseline (RMS) is a measure to quantify the amount of dispersion of the baseline due to noise. In Ch. 5.1, the baseline RMS was introduced as the standard deviation of the baseline, which itself is defined as the first 625 samples ($2.5\,\mu$s) of a waveform. Therefore, one can also think of the baseline RMS as the average noise amplitude of a waveform. Higher baseline RMS values indicate a greater deviation from the baseline and thus more noise. Using the data obtained from the waveform processing a histogram for each detector board's pixel is plotted. The plot sees the application of quality cuts, i.e., the rejection of pre-trace and in-trace pile-up events, see Fig. 39.

Contrary to expectations, from the plot the realization can be gained that the baseline RMS decreases with increasing distance between SDD and ASIC. As a result, the plot gives the impression that GIRAXO has the lowest noise, which is not the case, as will be seen in the analysis of the noise curves in Ch. 5.5.2. There are two possible explanations for this anomalous behavior. The first attempt at explanation takes into account the finding from Ch. 5.2 that GIRAXO exhibited a lower gain during the measurements. This would not only cause the offset of the uncalibrated spectra as previously seen, but also a general reduction in the amplitude of any waveform. As a result, noise-induced fluctuations around the baseline of a waveform are reduced, leading to a lower baseline RMS. However, this does not explain the behavior of Long, which has, in contrast to GIRAXO, no discernible difference in gain when compared to Short. Nevertheless, Long has a lower baseline RMS than Short. The second explanation is a different frequency response for each

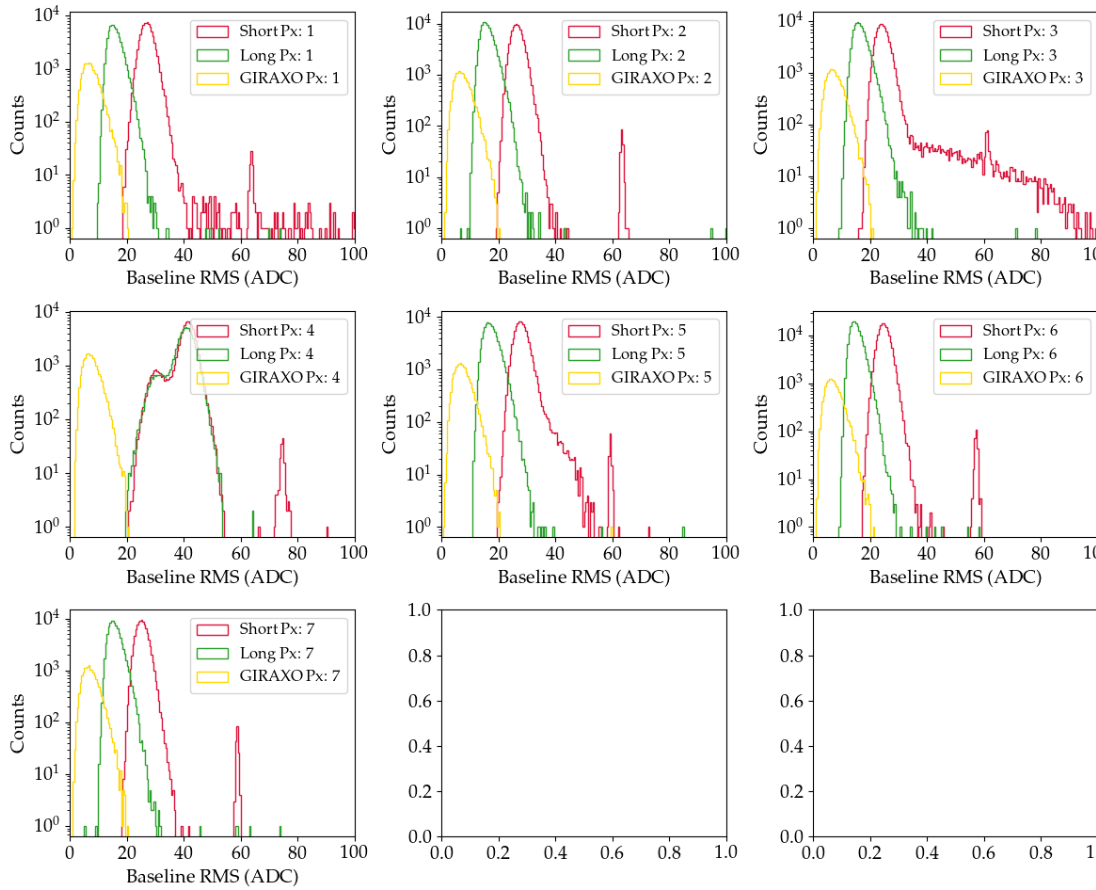

Figure 39: Baseline RMS distributions for each pixel of Short (red), Long (green), and GIRAXO (yellow). The obvious finding that the two longer boards have lower baseline RMS values than Short must be treated with caution and analyzed in future measurements further.

detector board. This could be due to the longer traces acting as a low pass filter, which would reduce the frequency response, making both Long and GIRAXO "blind" to this noise component. To verify this, the noise density spectra of the different detector boards will be investigated, outside the scope of this thesis.

When comparing the individual pixels in Fig. 39, one finds for Long and GIRAXO a similar performance throughout the pixels, except pixel 5 of Long. It exhibits an unusual behavior, as does pixel 5 of Short. Furthermore, pixel 5 of Short features additional counts in higher ADC values, as does pixel 5 to a lesser extent. This can be attributed to another population of events or external factors on that signal line, which will be investigated outside the scope of this thesis.

From the data of the baseline RMS distributions the mean and median value of each pixel is computed and then plotted in Fig 40. This enables a more direct comparison of the corresponding pixels. The plot only confirms previous findings. The previously mentioned unusual behavior of pixel 5 of Short and Long manifests in both as the respective worst performance of each board, regarding baseline RMS. There seems to be no correlation with the obtained FWHMs of Fig. 35.

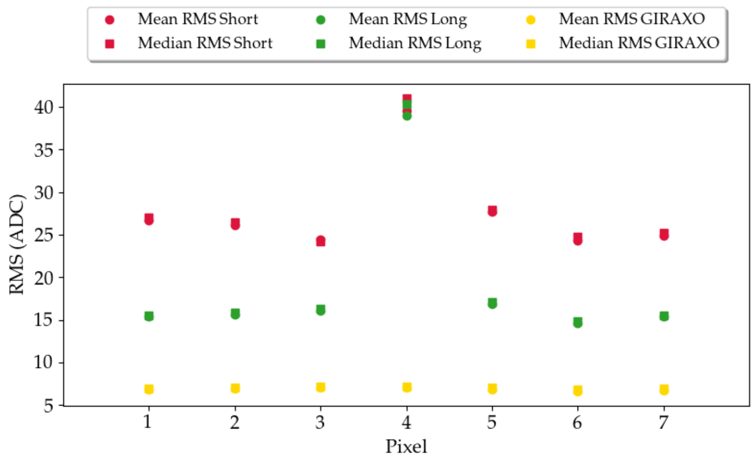

Figure 40: Comparison of mean and median baseline RMS of Short, Long and GIRAXO.

5.5.2 Noise curves

The different noise components (Ch. 5.4) depend on the time constants of the trapezoidal filter, specifically the filter rise time. As explained in Ch. 5.1, the trapezoidal filter is used to reconstruct the energy of the events for filter rise times ranging between $0.2\,\mu$s and $4.0\,\mu$s, resulting in ten spectra for each pixel. The FWHM is then computed for each spectrum, allowing one to relate the FWHM to the filter rise time. This dependency results in the noise curves for each pixel of a detector board. Subsequently, a mean noise curve is formed for each PCB, see Fig. 41. A noise curve is, in essence, a scan of the resolution over the filter rise time.

For all PCBs compared, the optimal filter rise time that minimizes total noise contribution is $2.0\,\mu$s. All house internally produced PCBs exhibit a significant increase in noise when compared to the XGLab board, which manages $\approx 205\,$eV at the same filter rise time. This increment concerns especially the amount of 1/f noise, which can be seen as an offset of the noise curves in the y direction. The increased occurrence of 1/f noise on the GIRAXO PCB indicates increased parasitic capacitance in the signal loop. This is to be expected given the longer traces in the signal loop, and it is further supported by the slope of its noise curve at shorter filter rise times. The slope increases with thermal noise, the amount of which increases with capacitance in the signal loop. The noise of the GIRAXO PCB increased dramatically for filter rise times shorter than $1.0\,\mu$s. As a result, its noise curve is restricted to this value. The effects of the thermal noise can also be seen, although less pronounced for the Long PCB. The amount of shot noise, which is related to the slope at longer filter rise times, is for all PCBs similar. Cooling the SDD decreases the amount of shot noise, which would flatten the curve at longer filter rise times. The conclusion that can be drawn is that the amount of 1/f noise and thermal noise increases with the length of traces in the signal loop. Nevertheless, the noise performance of GIRAXO is more than good enough for the use in IAXO.

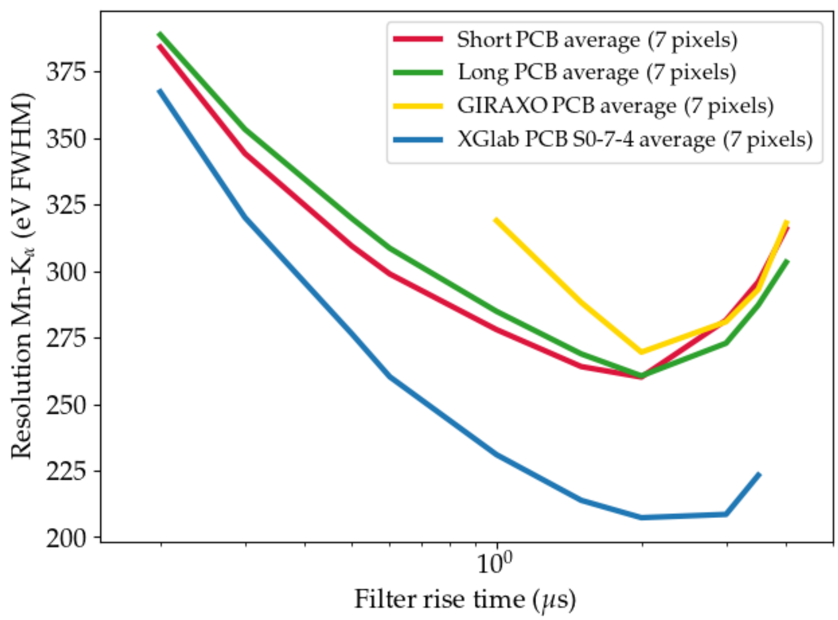

Figure 41: Noise curves: the measured FWHM as a function of energy filter rise time. The filter flot top time remained constant at $0.2\,\mu$s for Short and Long, and for GIRAXO at $0.5\,\mu$s. The performance of the Short (red line), Long (green line), and the GIRAXO PCB (yellow line) is compared at room temperature. The XGL-JFET-7CH-CARRIER board (blue line) serves as the baseline for the comparison. For the internally produced PCB the amount of 1/f noise is greater. The contribution of thermal noise increases with the distance between the SDD and the readout ASIC. For the GIRAXO PCB, this is more prevalent.

6 Background demonstrator

The GIRAXO PCB used in the scope of this thesis is a prototype PCB for a background demonstrator that will be operated at the Canfranc underground laboratory. All design decisions for the PCB were made to achieve the best possible background performance. The required background for BabyIAXO is $10^{-7}\,\mathrm{counts\,keV^{-1}\,cm^{-2}\,s^{-1}}$. In 2021 the latest background measurements with TRISTAN SDDs where made by our group, reaching a background of $(1.9 \pm 0.2) \cdot 10^{-5}\,\mathrm{counts\,keV^{-1}\,cm^{-2}\,s^{-1}}$ at the Unterground lab of the Technische Universität München [42]. The majority of the observed background was attributed to close-by impurities. The detector board used in this measurement consisted of a TRISTAN SDD with a readout CUBE preamplifier ASIC. The CUBEs are bonded directly to the anode of the SDD, which has the consequence that all of the electronics have to be in close proximity to the SDD.

6.1 GIRAXO PCB Design

The GIRAXO PCB incorporates a JFET and a readout ETTORE ASIC. This allows us to increase the distance between the SDD and the ASIC in order to place passive shielding between the two, blocking radiation emitted by the electronics. The GIRAXO PCB can be structured in three sections:

1. The head, which holds the SDD.
2. The neck, which connects the head to the rest of the body.
3. The body, which holds the ETTORE ASIC, electronics, and connectors.

In order to reduce radioactive contamination, the PCB material around the SDD is minimized. This includes the omission of solder mask on the head. Furthermore, the head protrudes perpendicular to the body. As a result, there is no direct line of sight between the SDD and the electronics, allowing us to place passive shielding between the two. When minimizing the head dimensions, the $250\,\mu\mathrm{m}$ wide high-voltage traces BF and BC that run around the SDD must be considered. Since their contacts are on the western SDD side, opposite to all other bonding pads, the traces have to be routed around the SDD. In addition, 2.5 mm of excess PCB material is planned north and south of the SDD, required for the holding structure of the PCB. Overall, this resulted in a head size of approximately $18\,\mathrm{mm} \times 35\,\mathrm{mm}$. The SDD is $12\,\mathrm{mm} \times 11\,\mathrm{mm}$ in size. A layout of the head is depicted in Fig. 42.

Traces that run from the SDD to the body pass through the neck. This includes the SDD and signal loop supply voltages. Signal lines belonging to different pixels are separated by a distance of 1.5 mm. This meant that the neck could be a minimum of 15 mm wide. The average length of the signal loop traces is 100 mm. This value was chosen because it allows for 70 mm of shielding between the SDD and the electronics. Compared to the first Short/Long prototype PCBs, the GIRAXO features the positioning of probing points and a more uniform component placement. The layout of the whole GIRAXO PCB is shown in Fig. 43.

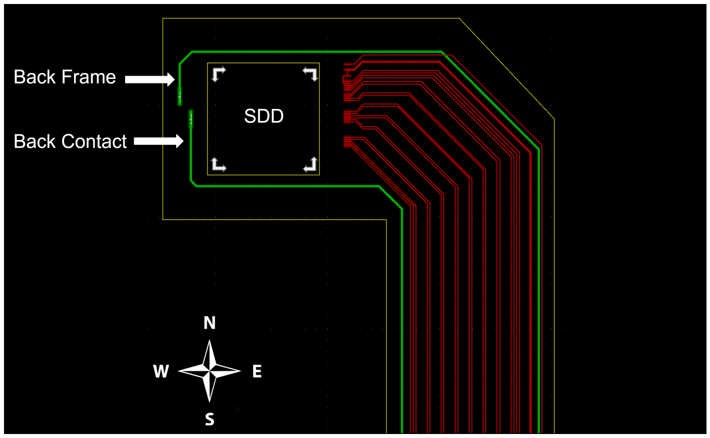

Figure 42: Layout of the PCB head The SDD is placed on the PCB head. Traces marked in red are placed on the copper top layer. This includes the traces for the signal loop and most of the supply voltages for the SDD. Traces marked in green are placed on the copper bottom

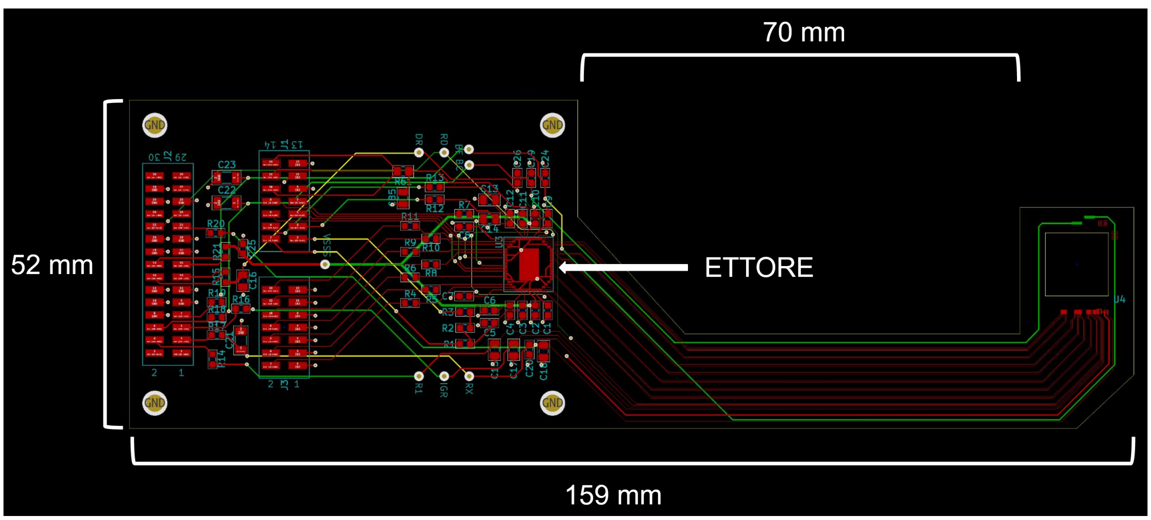

Figure 43: Layout of the GIRAXO PCB. The shape of the neck allows the placement of shielding between SDD and electronics. The traces that run from SDD to ASIC are approximately 100 mm long.

The GIRAXO PCB that will be used in the upcoming background demonstrator uses as substrate ARLON 85N, which is expected to be sufficient in radio-purity and is currently undergoing radio-assay measurements. A similar material was used by the EDELWEISS experiment that searches for dark matter search using cryogenic heat-and-ionization germanium detectors [59], and is going to be used in the upcoming Darkside experiment. Furthermore, the SDD is glued to the PCB with a low-background glue.

6.2 Passive shielding

The background demonstrator will be operated at Canfranc, which is an underground laboratory located in a abandoned train tunnel under Mount Tobazo. There, the setup will be placed at a depth of 2450 m.w.e., making muon-induced background irrelevant [60].

The PCB and its enclosure are housed in a lead castle within a flush box, which protects the setup from environmental radiation and results in ≈ 100 mm of lead coverage in all directions. Radon-free air or nitrogen gas will be used as a flush gas. Low activity lead will be used for the innermost bricks. To shield the SDD from the low-energy ^{210}Pb gamma rays, a box of low activity copper is used. The copper box serves simultaneously as a holding structure for the PCB and has the same dimensions as the lead bricks (200 mm $\times$ 100 mm $\times$ 50 mm). A 3D rendering of the copper holding structure is depicted in Fig. 44.

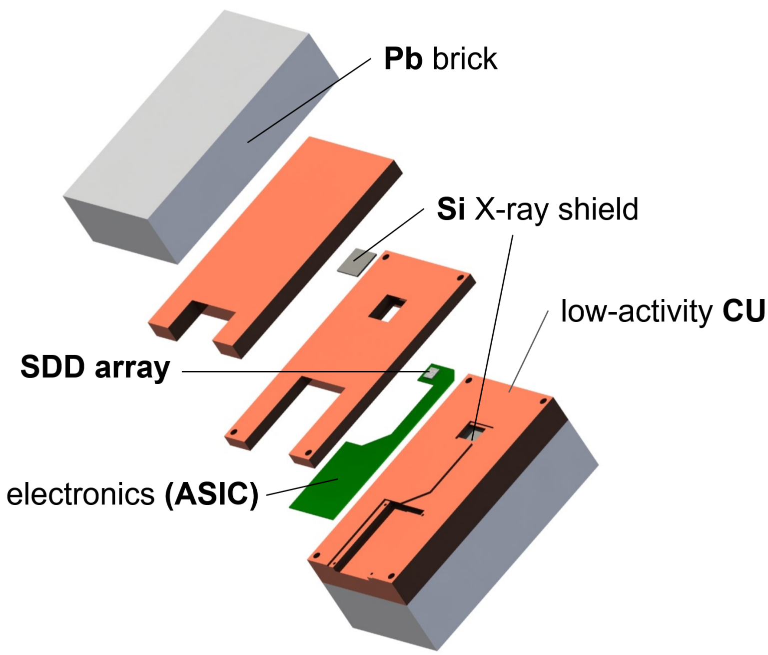

Figure 44: 3D rendering of the copper holding structure. The enclosure is placed inside a lead castle with a flush box. The copper brick houses the PCB and holds the silicon plates in position. The copper shields from ^{210}Pb decays, while the silicon plates shield from copper fluorescence.

This copper brick consists of three parts that can be assembled according to the building block principle. The three parts are held together by copper rods at the corners. The PCB is mounted in the lowest part. For this purpose, the copper is milled 1 mm deep so that the PCB can lie in the cutout. Due to the shape of the PCB, the head with the SDD is completely shielded from the intrinsic radiation of the rest of the PCB. A 5 mm deep cutout is located beneath the head of the PCB. This allows the placement of a 1.5 mm thick silicon plate that shields the SDD from the 8 keV fluorescence of copper. The remaining 3.5 mm of the cutout are planned as safety distance to the bonding wires of BF and BC, since they are located on the bottom side of the PCB. The middle section of the copper brick is placed on top of the lower section, sandwiching the PCB between the two. The middle section has cutouts directly over the SDD and the body of the PCB. The former allows for the addition of another silicon plate, resulting in nearly 4π of silicon coverage. The cutout above the body is essential to house the electrical components. The third part of the copper brick is the cover. It has a cutout over the body, which is required for cables that connect to the BIAS system. Overall, the SDD will be shielded by > 20 mm of copper. The benefit of the final design is that glue or screws that could cause radioactive background are avoided when mounting all components. A cross section of the copper brick is illustrated in Fig. 45.

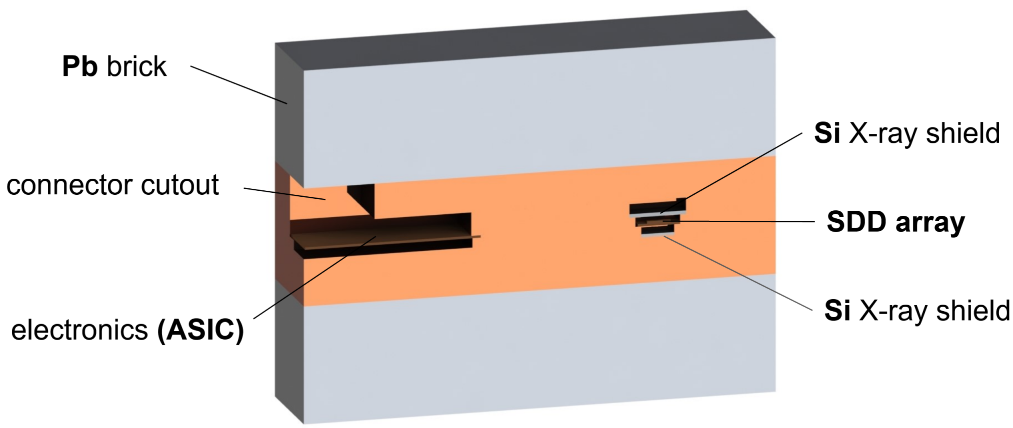

Figure 45: Cross section of assembled passive shielding. Cutouts in the copper part are milled above and beneath the SDD to accommodate silicon X-ray shielding. A cutout over the body of the PCB is milled to facilitate cable management. No glue or screws are required to secure the close-by components.

6.3 Background projections

Using the design of the setup and conservative radio-purity estimations for the individual parts, background projections were performed by our group. The SDD, PCB with electronics, and shielding were all separately modeled and then summed, as shown in Fig. 46. In the $0 - 10$ keV region of interest, the total background is expected to be $\sim 10^{-7}$ counts keV^{-1} cm^{-2} s^{-1}. The plot demonstrates that the background is mainly dominated by the contribution of the PCB with electronics. This emphasizes the importance of minimizing material around the head, which would be even easier if the TRISTAN SDDs had all bonding pads on the same side. Furthermore, the X-ray line at 8 keV indicates potential for improvement for the Silicon shielding. The line results from the fact, that the SDD is not fully enclosed in the silicon shield.

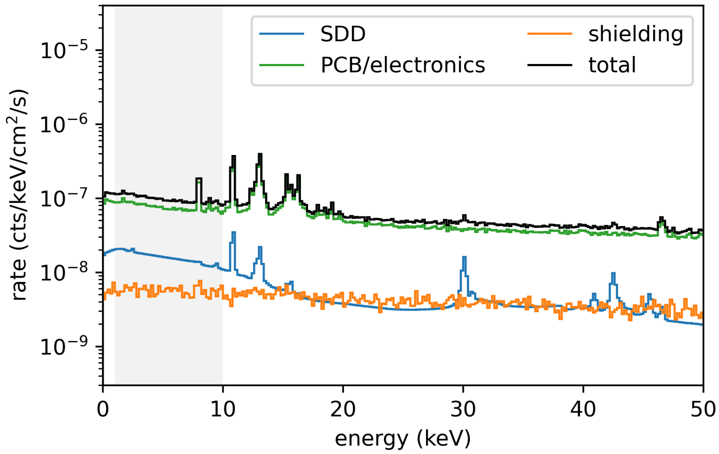

Figure 46: Background projections of the Canfranc background demonstrator. Conservative estimates project a total background (black line) of $\sim 10^{-7}\,\mathrm{counts\,keV^{-1}\,cm^{-2}\,s^{-1}}$ in the region of interest ($0 - 10\,\mathrm{keV}$).The depth of the Canfranc (2450 m.w.e.) renders muon-induced background irrelevant. The PCB head-area takes up the majority of the background (green line). The peak at 8 keV is the copper fluorescence line. The intrinsic background of the SDD (blue line) demonstrates the potential for even lower background levels. Provided by Christoph Wiesinger.

7 Conclusion and outlook

The IAXO experiment will search for axion-like particles originating from the Sun with the objective of probing axion couplings of a few $10^{-12}\,\mathrm{GeV}^{-1}$ for masses up to 0.25 eV, entering previously unexplored axion-like particle parameter space. This requires, among other things, the X-ray detectors to achieve a background level as low as $10^{-8}\,\mathrm{counts\,keV^{-1}\,cm^{-2}\,s^{-1}}$. For the first stage of the experiment, BabyIAXO, the baseline Micromegas detectors intend to reach a background level of $10^{-7}\,\mathrm{counts\,keV^{-1}\,cm^{-2}\,s^{-1}}$. The silicon drift detectors used by our group offer significant advantages for IAXO, as they outperform the baseline detector system in terms of energy resolution and X-ray efficiency. However, previous measurement campaigns were not yet capable of meeting the background requirements.

The primary focus of this thesis was the development of a prototype background demonstrator capable of exceeding previously set background levels. In particular, a detector board that incorporates a TRISTAN SDD with an integrated JFET was developed. Special emphasis was placed on the effects of the distance between the SDD and the readout ASIC. This distance was increased up to the point where radioactive impurities from the readout electronics can be shielded without compromising the performance of the detection system due to increased noise contributions. Three prototype PCBs with varying SDD/ASIC distances (15 mm, 75 mm, 100 mm) were produced and then characterized using a ^{55}Fe calibration source. The measured data was then processed using a classical pulse shape analysis approach, which allowed for a comparison of the performance of the detector boards.

First, the measured ^{55}Fe energy spectra were reconstructed, from which the energy resolution was subsequently computed. This was done for energy filters with varying shaping times. The analysis revealed no significant degradation in energy resolution with increasing SDD/ASIC distance. The final design of the detector board (GIRAXO) achieved an optimal energy resolution of 269 ± 9 eV at a filter flat top time of 0.5 μs and a filter rise time of 2.0 μs. In addition, the GIRAXO detector board experienced a decrease in gain, attributed to the large distance between the SDD and the ASIC. Furthermore, all detector boards featured an energy threshold of about 300 adc, the origin of which will be investigated in future measurements. In terms of keV, the GIRAXO board has a threshold of about 3 keV.
The noise curves for the detector boards were generated by the scanning the energy resolution over the filter rise times. A comparison with a commercially available detector board showed that all internally produced boards exhibit an increase in noise. Internally produced boards behave similarly to one another, with the exception of thermal noise, the amount of which increases with the SDD/ASIC distance. Furthermore, as was to be expected, the detector boards with longer SDD/ASIC distance experienced a significant increase in signal rise time. The GIRAXO PCB achieved a mean signal rise time of (251 ± 3) ns. This value meets the requirements as IAXO does not require a high count rate. The baseline RMS results deviate from expectations, as the longer PCBs achieved lower values. A future investigation of the noise density spectra will look for an explanation for this phenomenon.

As a final part of this thesis, a prototype for a dedicated passive shield for the GIRAXO PCB was designed. It consists of a three-part copper enclosure that holds the GIRAXO PCB and silicon X-ray shields. A radio-pure version of the GIRAXO PCB and the dedicated passive shield will be used in an upcoming measurement campaign at the Canfranc underground laboratory. The Canfranc background demonstrator is projected to achieve a total background of $\sim 10^{-7}\,\mathrm{counts\,keV^{-1}\,cm^{-2}\,s^{-1}}$. This thesis thus presents a background demonstrator design for the TRISTAN SDDs that, if projections are met in the upcoming Canfranc measurements, will satisfy the background requirements for BabyIAXO while also achieving good energy resolution.

References

[1] National Aeronautics and Space Administration. Dark energy, dark matter. https://science.nasa.gov/astrophysics/focus-areas/what-is-dark-energy. Accessed: 2022-06-30.

[2] Susanne Mertens, Antonio Alborini, Konrad Altenmüller, Tobias Bode, Luca Bombelli, Tim Brunst, Marco Carminati, David Fink, Carlo Fiorini, Thibaut Houdy, et al. A novel detector system for katrin to search for kev-scale sterile neutrinos. *Journal of Physics G: Nuclear and Particle Physics*, 46(6):065203, 2019.

[3] Joerg Jaeckel and Javier Redondo. Resonant to broadband searches for cold dark matter consisting of weakly interacting slim particles. *Physical Review D*, 88(11):115002, 2013.

[4] Cumrun Vafa and Edward Witten. Parity conservation in quantum chromodynamics. *Physical Review Letters*, 53(6):535, 1984.

[5] David JE Marsh. Axions and alps: a very short introduction. *arXiv preprint arXiv:1712.03018*, 2017.

[6] RJ Crewther, P Di Vecchia, G Veneziano, and Edward Witten. Chiral estimate of the electric dipole moment of the neutron in quantum chromodynamics. *Physics Letters B*, 88(1-2):123–127, 1979.

[7] JM Pendlebury, Samer Afach, Nicholas J Ayres, Charles A Baker, Gilles Ban, Georg Bison, Kazimierz Bodek, Martin Burghoff, Peter Geltenbort, Katie Green, et al. Revised experimental upper limit on the electric dipole moment of the neutron. *Physical Review D*, 92(9):092003, 2015.

[8] Elisa Ruiz Chóliz. *Ultra-low background microbulk micromegas x-ray detectors for axion searches in iaxo and babyiaxo*. PhD thesis, Universidad de Zaragoza, 2019.

[9] Rohit Verma. Quark mass matrices, textures and ckm precision measurements. *International Journal of Modern Physics A*, 32(25):1750151, 2017.

[10] Roberto D Peccei. The strong cp problem and axions. In *Axions*, pages 3–17. Springer, 2008.

[11] R. D. Peccei and Helen R. Quinn. CP conservation in the presence of pseudoparticles. *Phys. Rev. Lett.*, 38:1440–1443, Jun 1977.

[12] Igor G Irastorza. An introduction to axions and their detection. *arXiv preprint arXiv:2109.07376*, 2021.

[13] J Noronha-Hostler, H Ahmad, J Noronha, and C Greiner. Particle ratios as a probe of the qcd critical temperature. *Physical Review C*, 82(2):024913, 2010.

[14] Y Asano, E Kikutani, S Kurokawa, T Miyachi, M Miyajima, Y Nagashima, T Shinkawa, S Sugimoto, and Y Yoshimura. Search for a rare decay mode k$+\to\pi+\nu$v and axion. *Physics Letters B*, 107(1-2):159–162, 1981.

[15] Mikhail A Shifman, AI Vainshtein, and Valentin I Zakharov. Can confinement ensure natural cp invariance of strong interactions? *Nuclear Physics B*, 166(3):493–506, 1980.

[16] Jihn E Kim. Weak-interaction singlet and strong cp invariance. *Physical Review Letters*, 43(2):103, 1979.

[17] Michael Dine, Willy Fischler, and Mark Srednicki. A simple solution to the strong cp problem with a harmless axion. *Physics letters B*, 104(3):199–202, 1981.

[18] SL Cheng, CQ Geng, and W-T Ni. Axion-photon couplings in invisible axion models. *Physical Review D*, 52(5):3132, 1995.

[19] Javier Redondo. Solar axion flux from the axion-electron coupling. *Journal of Cosmology and Astroparticle Physics*, 2013(12):008, 2013.

[20] JL Hewett, H Weerts, R Brock, JN Butler, BCK Casey, J Collar, A de Gouvea, R Essig, Y Grossman, W Haxton, et al. Fundamental physics at the intensity frontier. *arXiv preprint arXiv:1205.2671*, 2012.

[21] K Baker, Giovanni Cantatore, SA Cetin, M Davenport, K Desch, B Döbrich, H Gies, IG Irastorza, J Jaeckel, A Lindner, et al. The quest for axions and other new light particles. *Annalen der Physik*, 525(6):A93–A99, 2013.

[22] Nicolás Viaux, Márcio Catelan, Peter B Stetson, GG Raffelt, Javier Redondo, Aldo AR Valcarce, and Achim Weiss. Neutrino and axion bounds from the globular cluster m5 (ngc 5904). *Physical Review Letters*, 111(23):231301, 2013.

[23] David N Spergel, R Bean, O Doré, MR Nolta, CL Bennett, Joanna Dunkley, G Hinshaw, N ea Jarosik, E Komatsu, L Page, et al. Three-year wilkinson microwave anisotropy probe (wmap) observations: implications for cosmology. *The Astrophysical Journal Supplement Series*, 170(2):377, 2007.

[24] Andreas Ringwald. Exploring the role of axions and other wisps in the dark universe. *Physics of the Dark Universe*, 1(1-2):116–135, 2012.

[25] Fritz Zwicky. The redshift of extragalactic nebulae. *Helvetica Physica Acta*, 6:110–127, 1933.

[26] Riccardo Murgia, Stefano Gariazzo, and Nicolao Fornengo. Constraints on the coupling between dark energy and dark matter from cmb data. *Journal of Cosmology and Astroparticle Physics*, 2016(04):014, 2016.

[27] Richard Massey, Thomas Kitching, and Johan Richard. The dark matter of gravitational lensing. *Reports on Progress in Physics*, 73(8):086901, 2010.

[28] Pierre Sikivie. Experimental tests of the" invisible" axion. *Physical Review Letters*, 51(16):1415, 1983.

[29] H Peng, S Asztalos, E Daw, NA Golubev, C Hagmann, D Kinion, J LaVeigne, DM Moltz, F Nezrick, J Powell, et al. Cryogenic cavity detector for a large-scale cold dark-matter axion search. *Nuclear Instruments and Methods in Physics Research Section A: Accelerators, Spectrometers, Detectors and Associated Equipment*, 444(3):569–583, 2000.

[30] SJ Asztalos, G Carosi, C Hagmann, D Kinion, K Van Bibber, M Hotz, LJ Rosenberg, G Rybka, A Wagner, J Hoskins, et al. Design and performance of the admx squid-based microwave receiver. *Nuclear Instruments and Methods in Physics Research Section A: Accelerators, Spectrometers, Detectors and Associated Equipment*, 656(1):39–44, 2011.

[31] Stephen J Asztalos, RF Bradley, L Duffy, C Hagmann, D Kinion, DM Moltz, LJ Rosenberg, P Sikivie, W Stoeffl, NS Sullivan, et al. Improved rf cavity search for halo axions. *Physical Review D*, 69(1):011101, 2004.

[32] Stephen J Asztalos, G Carosi, C Hagmann, D Kinion, K Van Bibber, M Hotz, LJ Rosenberg, G Rybka, J Hoskins, J Hwang, et al. Squid-based microwave cavity search for dark-matter axions. *Physical review letters*, 104(4):041301, 2010.

[33] Babette Döbrich. Bsm photon interaction for alps-ii and beyond. *arXiv preprint arXiv:1212.2770*, 2012.

[34] Klaus Ehret, Maik Frede, Samvel Ghazaryan, Matthias Hildebrandt, Ernst-Axel Knabbe, Dietmar Kracht, Axel Lindner, Jenny List, Tobias Meier, Niels Meyer, et al. New alps results on hidden-sector lightweights. *Physics Letters B*, 689(4-5):149–155, 2010.

[35] Robin Bähre, Babette Döbrich, Jan Dreyling-Eschweiler, Samvel Ghazaryan, Reza Hodajerdi, Dieter Horns, Friederike Januschek, E-A Knabbe, Axel Lindner, Dieter Notz, et al. Any light particle search ii—technical design report. *Journal of Instrumentation*, 8(09):T09001, 2013.

[36] E Armengaud, FT Avignone, M Betz, P Brax, P Brun, Giovanni Cantatore, JM Carmona, GP Carosi, F Caspers, S Caspi, et al. Conceptual design of the international axion observatory (iaxo). *Journal of Instrumentation*, 9(05):T05002, 2014.

[37] DM Lazarus, GC Smith, R Cameron, AC Melissinos, G Ruoso, Yannis K Semertzidis, and FA Nezrick. Search for solar axions. *Physical Review Letters*, 69(16):2333, 1992.

[38] Igor G Irastorza, FT Avignone, A Liolios, S Russenschuck, H ten Kate, K van Bibber, T Geralis, O Limousin, JA Villar, H Gomez, et al. The international axion observatory iaxo. letter of intent to the cern sps committee. Technical report, 2013.

[39] Theopisti Dafni and Javier Galán. Digging into axion physics with (baby) iaxo. *Universe*, 8(1):37, 2022.

[40] National Aeronautics and Space Administration. X-ray optics. https://universe.gsfc.nasa.gov/xrays/MirrorLab/xoptics.html, 2012. Accessed: 2022-06-16.

[41] Igor G Irastorza, FT Avignone, S Caspi, JM Carmona, T Dafni, M Davenport, A Dudarev, G Fanourakis, E Ferrer-Ribas, J Galán, et al. Towards a new generation axion helioscope. *Journal of Cosmology and Astroparticle Physics*, 2011(06):013, 2011.

[42] Thibaut Houdy. A tristan module as a solar axion detector. 2021.

[43] Tim Benjamin Brunst. *First generation prototype detectors for the TRISTAN project.* PhD thesis, Technische Universität München, 2020.

[44] P Lechner, C Fiorini, R Hartmann, J Kemmer, N Krause, P Leutenegger, A Longoni, H Soltau, D Stötter, R Stötter, et al. Silicon drift detectors for high count rate x-ray spectroscopy at room temperature. *Nuclear Instruments and Methods in Physics Research Section A: Accelerators, Spectrometers, Detectors and Associated Equipment*, 458(1-2):281–287, 2001.

[45] MN Mazziotta et al. Electron-hole pair creation energy and fano factor temperature dependence in silicon. *Nuclear instruments & methods in physics research. Section A, Accelerators, spectrometers, detectors and associated equipment*, 584(2):436, 2008.

[46] William R Leo. Techniques for nuclear and particle physics experiments: A how-to approach, 1994.

[47] Daniel Benedikt Siegmann. Investigation of the detector response to electrons of the tristan prototype detectors. Master's thesis, 2019.

[48] Thibaut Houdy. Tristan silicon drift prototype as iaxo detector. 2019.

[49] Shuo Wang and Fred C Lee. Analysis and applications of parasitic capacitance cancellation techniques for emi suppression. *IEEE Transactions on Industrial Electronics*, 57(9):3109–3117, 2009.

[50] Jakov Kholdkov. Measurement of adc nonlinearities and development of a bias board for the tristan detector. Master's thesis, 2021.

[51] Georges Audi, Olivier Bersillon, Jean Blachot, and Aaldert Hendrik Wapstra. The nubase evaluation of nuclear and decay properties. *Nuclear physics A*, 729(1):3–128, 2003.

[52] Laboratoire National Henri Becquerel. Table de radionucléides. `http://www.nucleide.org/DDEP_WG/Nuclides/Fe-55_tables.pdf`, 2006. Accessed: 2022-06-15.

[53] Frank Arne Edzards. *Characterization of point contact Germanium detectors and development of signal readout electronics for LEGEND.* PhD thesis, Technische Universität München, 2021.

[54] Ronald W Schafer. What is a savitzky-golay filter?[lecture notes]. *IEEE Signal processing magazine*, 28(4):111–117, 2011.

[55] Tobias Eggert. *Die spektrale Antwort von Silizium-Röntgendetektoren.* PhD thesis, Technische Universität München, 2004.

[56] Gregory Y Prigozhin, Andrew P Rasmussen, Mark W Bautz, and George R Ricker Jr. Model of the x-ray response of the acis ccd. In *X-Ray Optics, Instruments, and Missions*, volume 3444, pages 267–275. SPIE, 1998.

[57] Hermann Kolanoski and Norbert Wermes. *Teilchendetektoren.* Springer, 2016.

[58] Felix A Levinzon and LKJ Vandamme. Comparison of 1/f noise in jfets and mosfets with several figures of merit. *Fluctuation and Noise Letters*, 10(04):447–465, 2011.

[59] Veronique Sanglard, Alain Benoit, L Bergé, J Blümer, A Broniatowski, B Censier, L Chabert, M Chapellier, G Chardin, P Charvin, et al. Final results of the edelweiss-i dark matter search with cryogenic heat-and-ionization ge detectors. *Physical Review D*, 71(12):122002, 2005.

[60] Susana Cebrian. Double beta decay experiments at canfranc underground laboratory. *Progress in Particle and Nuclear Physics*, 114:103807, 2020.

A PCB design and production

Reference	Footprint	Value	Reference	Footprint	Value
C1	C_0603_1608Metric	100nF	R1	R_0603_1608Metric	0
C2	C_0603_1608Metric	100nF	R2	R_0603_1608Metric	DNP
C3	C_0603_1608Metric	100nF	R3	R_0603_1608Metric	0
C4	C_0603_1608Metric	100nF	R4	R_0603_1608Metric	47
C5	C_0603_1608Metric	10uF	R5	R_0603_1608Metric	47
C6	C_0603_1608Metric	10uF	R6	R_0603_1608Metric	47
C7	C_0603_1608Metric	100nF	R7	R_0603_1608Metric	75
C8	C_0603_1608Metric	100nF	R8	R_0603_1608Metric	47
C9	C_0603_1608Metric	100nF	R9	R_0603_1608Metric	47
C10	C_0603_1608Metric	100nF	R10	R_0603_1608Metric	47
C11	C_0603_1608Metric	100nF	R11	R_0603_1608Metric	47
C12	C_0603_1608Metric	100nF	R12	R_0603_1608Metric	0
C13	C_0805_2012Metric	10uF	R13	R_0603_1608Metric	0
C14	C_0805_2012Metric	10uF	R14	R_0603_1608Metric	4.7k
C15	C_0805_2012Metric	1uF	R15	R_0603_1608Metric	47
C16	C_0805_2012Metric	10uF	R16	R_0603_1608Metric	22k
C17	C_0805_2012Metric	1uF	R17	R_0603_1608Metric	4.7k
C18	C_0805_2012Metric	10uF	R18	R_0603_1608Metric	22k
C19	C_0603_1608Metric	10nF	R19	R_0603_1608Metric	22k
C20	C_0603_1608Metric	10nF	R20	R_0603_1608Metric	10k
C21	C_1206_3216Metric	1uF	R21	R_0603_1608Metric	47
C22	C_1206_3216Metric	1uF	R61	R_0805_2012Metric	0
C23	C_1206_3216Metric	1uF			
C24	C_0603_1608Metric	10nF			
C25	C_0603_1608Metric	10uF			
C26	C_0603_1608Metric	100nF			
C85	C_0805_2012Metric	4.7uF			

B Data acquisition software settings

Run Number	32	14	36
PCB	short	long	GIRAXO
DAQ	CAEN desktop	CAEN desktop	CAEN desktop
Pulser	no	no	no
Acquisition mode	waves	waves	waves
Record length	5 min	5 min	5 min
Trace length	20000 ns	20000 ns	20000 ns
Pre-trigger	4000 ns	4000 ns	4000 ns
Polarity	negative	negative	negative
N samples baseline	256 samples	256 samples	256 samples
DC Offset	80 %	80 %	80 %
Course gain	1x	1x	1x
Threshold	100 lsb	50 lsb	50 lsb
Trigger holdoff	192 ns	192 ns	192 ns
Fast Disc. smoothing	64 samples	128 samples	128 samples
Input risetime	96 ns	192 ns	192 ns
Trap. rise time	2,992 us	2.992 us	2.992 us
Trap. flat top	0.192 us	0.288 us	0.288 us
Trap. pole zero	14.992 us	14.992 us	14.992 us
Peaking time	83.3 %	83.3 %	83.3 %
N samples peak	1 sample	1 sample	1 sample
Peak holdoff	0.992 us	0.992 us	0.992 us

Acknowledgments

First and foremost, I would like to thank Prof. Dr. Susanne Mertens for allowing me to work on my thesis in her group. The time was a wonderful opportunity to learn a variety of skills, and it far exceeded my expectations.

I would like to express my gratitude to Dr. Frank Edzards for his constant encouragement and active involvement throughout the creation of this work. When questions arose, he was always available to explain concepts, principles, and experimental methods in a very understandable manner, as well as their corresponding validity within the scope of this thesis.

I would also like to thank Dr. Christoph Wiesinger for the numerous fruitful discussions that resulted in the design of the background demonstrator, the constructive feedback, and detailed answers to all my questions.

In addition to this, I would like to thank Korbinian Urban for giving me an introduction to PCB design and noise theory.

Finally, I would like to thank the entire KATRIN and TRISTAN group for the wonderful working environment, lunchtime discussions, and numerous group activities that made my time at the MPP memorable.